Karlsruhe Institute of Technology

Annual Report 2022

Institute for Pulsed Power and Microwave Technology
Institut für Hochleistungsimpuls- und Mikrowellentechnik

John Jelonnek (ed)

Annual Report 2022

Institute for Pulsed Power and Microwave Technology
Institut für Hochleistungsimpuls- und Mikrowellentechnik

John Jelonnek (ed)

Part of this work has been carried out within the framework of the EUROfusion Consortium, funded by the European Union via the Euratom Research and Training Programme (Grant Agreement No 101052200 — EUROfusion). Views and opinions expressed are however those of the author(s) only and do not necessarily reflect those of the European Union or the European Commission. Neither the European Union nor the European Commission can be held responsible for them.

Part of the simulations presented in this work have been carried out by using the HELIOS supercomputer at IFERC-CSC.

Impressum
Karlsruher Institut für Technologie (KIT)

KIT – Die Forschungsuniversität in der Helmholtz-Gemeinschaft

Institute for Pulsed Power and Microwave Technology (IHM)

Institut für Hochleistungsimpuls- und Mikrowellentechnik (IHM)

Director: Prof. Dr.-Ing. John Jelonnek

The Institute for Pulsed Power and Microwave Technology (Institut für Hochleistungsimpuls- und Mikrowellentechnik, IHM) is working in the areas of pulsed power and high-power microwave technologies. Both, research and development of high power sources as well as related applications are in the focus. Applications for pulsed power technologies are ranging from materials processing to bioelectrics. High power microwave technologies are focusing on microwave sources (gyrotrons) for electron cyclotron resonance heating of magnetically confined plasmas and on applications for materials processing at microwave frequencies.

IHM is doing research, development, academic education, and, in close collaboration with the KIT division IMA and industrial partners, technology transfer. The focus is on the long-term goals of the Helmholtz Association of German Research Centres (HGF). During the currently running Program-Oriented Funding period (POF4), IHM is doing research work in the HGF programs “Nuclear Fusion (FUSION)”, “Nuclear Waste Management, Safety and Radiation Research (NUSAFE)” and “Materials and Technologies for the Energy Transition (MTET)”.

Projects funded by third-parties complement significantly the research work within all the different HGF programs. Considering the pulsed power technology and related applications, that includes the research on e. g. microalgae processing at large-scale relevant for industrial processes, the PEF-assisted extraction of valuable compounds and the development of powerful semiconductor-based marx-type pulse generators. Additionally, it includes the development of new materials that mitigate corrosion while being in contact with liquid metals and salts as required for future liquid metal batteries and the technical feasibility and scaling of CO_2-free methane pyrolysis in liquid high-temperature Sn respectively.

Considering the application of high-power microwaves to new and innovative energy-efficient industrial processes, third-party projects include the research on e. g. microwave assisted intermittent pultrusion of CFRP profiles, microwave assisted additive manufacturing with continuous carbon fiber reinforced thermoplastic filaments and the controlling and demolition of the distribution of weeds in crop fields.

All research areas are strongly interdisciplinary and require the profound knowledge on modern electron beam optics, high power microwave technologies, vacuum electronics, material technologies, high voltage technologies and high voltage measurement techniques.

Table of Contents

1 Nuclear Fusion (FUSION): Plasma Heating Systems - Microwave Plasma Heating & Current Drive Systems -

Contact: Dr. Gerd Gantenbein

The Department for High Power Microwave Technologies focuses on the research and development of high power microwave sources (gyrotrons) and related components for electron cyclotron resonance heating and current drive (ECRH&CD) of magnetically confined nuclear fusion plasmas. Additionally, it is strongly involved in the application oriented research in the field of microwave assisted dielectric heating and microwave plasmas.

In particular the following major activities have been carried out in 2022:

- Enabling Research Project funded by EUROfusion focusing on megawatt-class fusion gyrotron systems based on highly efficient operation at the second harmonic of the cyclotron frequency.
- Fundamental research on a gyro-travelling wave tube with a helically corrugated interaction region at 263 GHz and 1 kW for the SFB 1527 HyPERiON project.
- Innovative Concept of a Frequency-Doubling High-Power gyrotron traveling wave amplifier (FD-GTWT) with high gain over a broad bandwidth of 17.5 GHz at 263 GHz.
- Multistage Depressed Collectors as a key component for high efficiency operation of high power gyrotrons.
- Quasi-Optical mode converter, broadband window and Matching Optical Unit.
- Activities in DEMO EC system design and collaborations with DEMO physics towards a widely usable flight simulator for different tokamaks and configurations.
- Frequency-Stabilization of Megawatt-Class Gyrotrons with a phase -locked loop for Collective Thomson Scattering at W7-X.
- Start of operation of the new KIT gyrotron teststand FULGOR with a 1.5 MW 140 GHz short pulse gyrotron.
- Design activities of a 1 MW 105 GHz gyrotron for the CEA/WEST tokamak.

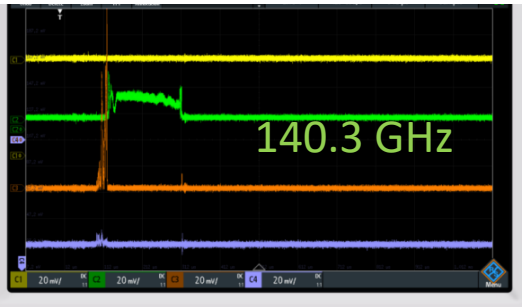

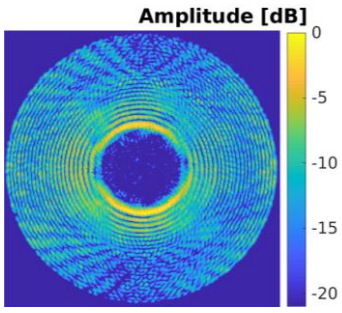

1.1 Key components verification and preparation of the first 2 MW 170/204 GHz coaxial-cavity short-pulse gyrotron

Contact: Dr.-Ing. Tobias Ruess

Future fusion machines might require gyrotrons operating above 200 GHz. Therefore, a first 2 MW 170/204 GHz coaxial-cavity short-pulse gyrotron pre-prototype has been designed on the basis of the 2 MW 170 GHz coaxial-cavity design. Dedicated gyrotron key components such as the Magnetron Injection Gun (MIG), the coaxial cavity and the quasi-optical output coupler were optimized. A validation of those components is necessary before installation into the gyrotron. Special remark is given by the automated mode generator for the verification of the quasi-optical output coupler. The $TE_{40,23}$ cavity mode operating at 204 GHz has been excited in cold test, as presented Fig. 1.1.1 (left). This mode is the highest mode, which has ever been excited in cold tests worldwide. Afterwards, this mode is used to verify the new quasi-optical output system. The measurement of the quasi-optical output coupler (launcher and beam forming mirrors) is presented in Fig. 1.1.1 (right). The measurements are in excellent agreement with the simulations.

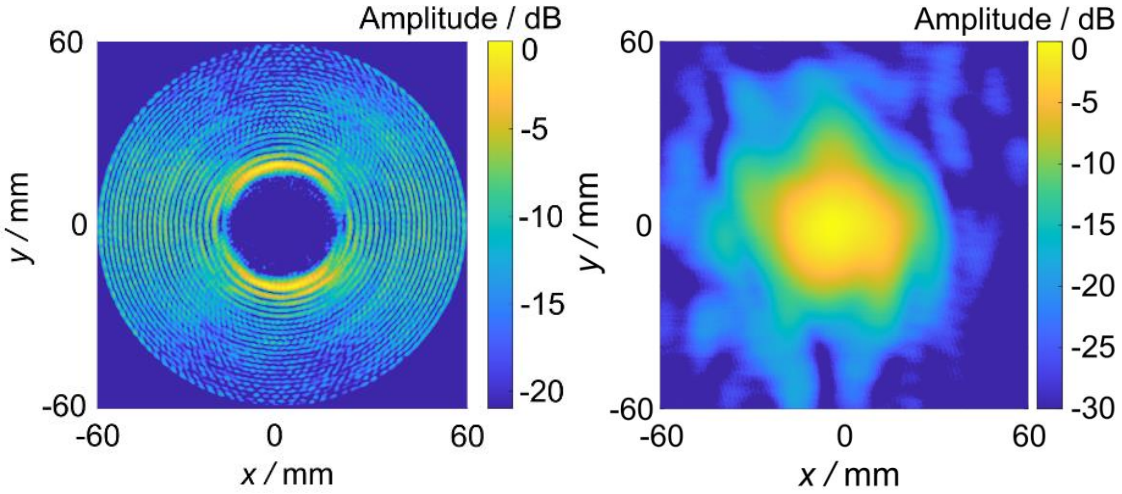

Fig. 1.1.1: Verification of the quasi-optical output coupler. Excitation of the $TE_{40,23}$ mode at 204 GHz in low power cold tests (left) and measurement of the Gaussian beam using the given cavity mode at the window plane (right) with a content of > 95 %.

The dimensions of the other components such as the anode, insert and cavity have been validated by a high-precision 3D measurement arm. Fig. 1.1.2 presents the assembled coaxial-cavity pre-prototype for the first proof-of-principal experiments at 170 GHz and 204 GHz (without collector on top)

The assembled 2 MW 170/204 GHz will be operated with a 10.5 T SC magnet which is under procurement. This magnet will provide the required maximum magnetic field strength for the operation at 204 GHz. This gyrotron will be the first gyrotron operated above 200 GHz in Europe.

Fig. 1.1.2: Preparation of the first 2 MW 170/204 GHz coaxial-cavity short-pulse pre-prototype (collector is missing).

1.2 EUROfusion Enabling Research (ENR)

Contact: Dr. Stefan Illy

Mid-2021 a new EUROfusion Enabling Research (ENR) project has been initiated in collaboration with the National and Kapodistrian University of Athens (NKUA). This project focuses on new concepts for highly efficient, megawatt-class fusion gyrotron systems that will operate at the second harmonic of the electron cyclotron frequency. This will reduce the required magnetic flux density by a factor of two and therefore will lead to more compact and cost-efficient gyrotron systems at DEMO relevant and sub-THz frequencies.

To form a basis for efficient and stable operation at the 2^{nd} harmonic, the following theoretical investigations have been performed during 2022:

Studies on mode locking to stabilize the operation at the second harmonic and to actively suppress the critical fundamental harmonic.

The design of a dual-beam quasi-optical launcher system which permits injection of the driving power for mode-locked operation. Both the so-called hybrid-type launcher and the mirror-line launcher have been investigated.

The possibility to stabilize the 2^{nd}-harmonic operation by using a corrugated insert and by applying also corrugations to the outer wall of the resonator. Two different possibilities have been investigated: (i) application of a corrugated insert only, based on the existing 170 GHz coaxial cavity gyrotron and (ii) application of inner and outer corrugations. In the latter case detailed investigations have been performed to find appropriate mode coupling schemes to suppress the critical fundamental competitor.

Simulations have been performed to check the possibility to use multi-stage depressed collectors to enhance the overall efficiency of second-harmonic gyrotrons. This investigation is based on an existing short-pulse collector design (for a fundamental-mode gyrotron) and the results clearly indicate that a significant efficiency enhancement will be also possible for second-harmonic gyrotrons.

Partly the activities focus on a relatively quick realization of a short-pulse high power second harmonic gyrotron. A new cavity for the existing KIT fundamental 170 GHz 2 MW gyrotron is designed, capable to operate at the second harmonic. The cavity is optimized in such way, that the currently available quasi-optical mode converter and electron gun can be used without major modifications. The corrugated insert and the cavity dimensions, which are shown in Fig. 1.2.1, are modified, wherease the operating mode $TE_{34,19}$ is kept the same as for the 170 GHz 2 MW coaxial-cavity gyrotron operating at fundamental harmonic of the electron cyclotron resonance frequency. The design allows theoretically close to 1.6 MW of output power, as shown in Fig. 1.2.2, while still complying with the maximum allowed ohmic wall loading of 2 $kWcm^{-2}$ at the cavity walls.

The special design method for the cavity is also applied to frequencies up to 280 GHz: It shall allow to extend the operational frequency range in the current available magnet systems.

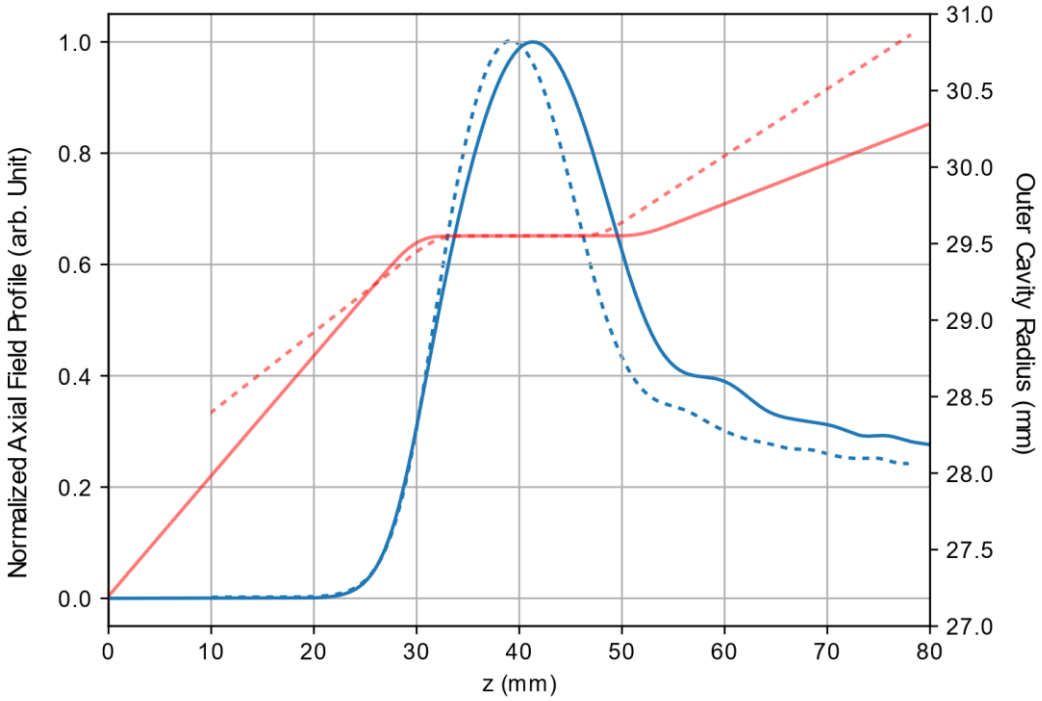

Fig. 1.2.1: Comparison of fundamental (--) and harmonic cavities (–) and field profiles of the operating mode

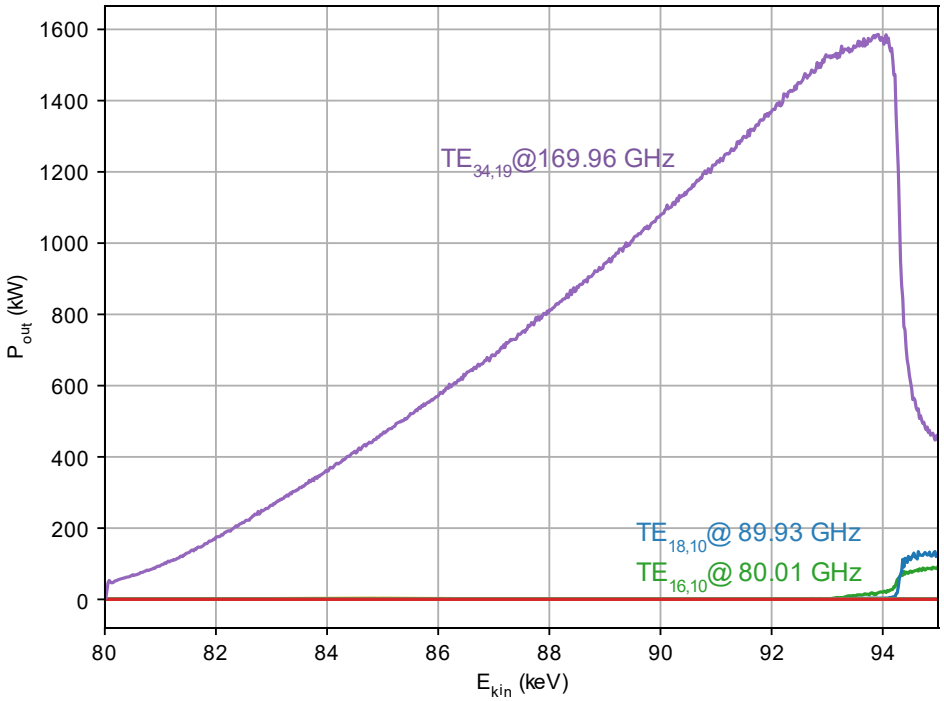

Fig. 1.2.2: Gyrotron output power vs kinetic particle energy at the cavity entrance

1.3 FULGOR

Contact: Dr. Gerd Gantenbein

FULGOR, the new KIT gyrotron teststand for megawatt-class gyrotrons has started its operation in 2022. The target parameters of the new gyrotron test facility will strongly support KIT's leading role in the development of advanced gyrotrons. It will help to answer the questions regarding the technical limits and new physical designs for future high-power microwave tubes.

The major subsections of FULGOR are:

- HV DC PS (High Voltage Direct Current Power Supply),
- 10.5 T superconducting magnet,
- Water cooling system,
- Advanced control system,
- Calorimetric and microwave diagnostics.

The HVDCPS (High Voltage Direct Current Power Supply) is built by Ampegon AG, CH. It takes advantage of the Enhanced Pulse Step Modulator technology which allows intermediate tapping points for highly efficient operation of gyrotrons with multi-staged depressed collectors and very low noise levels. The power supply is designed for 10 MW CW operation at 90 kV and 120 A, for short pulse operation (< 5 ms) 130 kV at 120 A is possible. Specific modular units make sure that in case of an arc in the gyrotron the energy is limited to 10 J. The rise time of the pulse is < 50 □s, the modulation frequency is up to 5 kHz.

An additional CW body power supply (BPS) for operation of conventional single-stage depressed collector gyrotrons has been installed. This power supply delivers an output voltage of up to 50 kV at 100 mA. An overview oft he complete system is given in Fig. 1.3.1.

First tests of the teststand FULGOR have been performed with a short pulse 1.5 MW, 140 GHz gyrotron. This tube has been extensively tested at IHM's old teststand and it is used as a reference to verify the proper operation of the new teststand. A new cryo-free superconducting 6 T magnet is used for these tests. Fig. 1.3.2 shows the installation of the gyrotron into the magnet. The gyrotron has been operated with parameters close to nominal (Ucathode ~ 70 – 85 kV, Ibeam~ 40 – 55 A) for ~ 1 ms. Without further optimization of the operating parameters the RF power achieved was 500 – 700 kW. Fig. 1.3.3 (top) shows first measurements of voltage and electron beam, Fig 4 (bottom) shows first microwave produced at the teststand FULGOR.

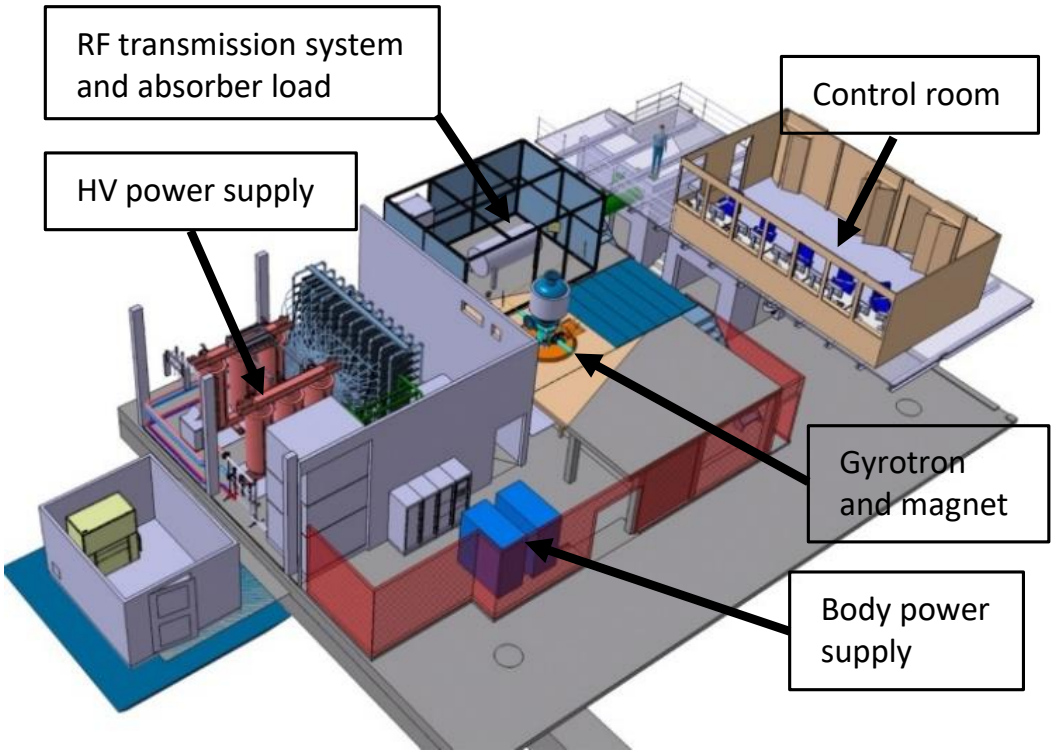

Fig. 1.3.1: CAD view of FULGOR teststand and microwave box with transmission system and RF dummy load.

Fig. 1.3.2: Installation of a short pulse 1.5 MW 140 GHz gyrotron.

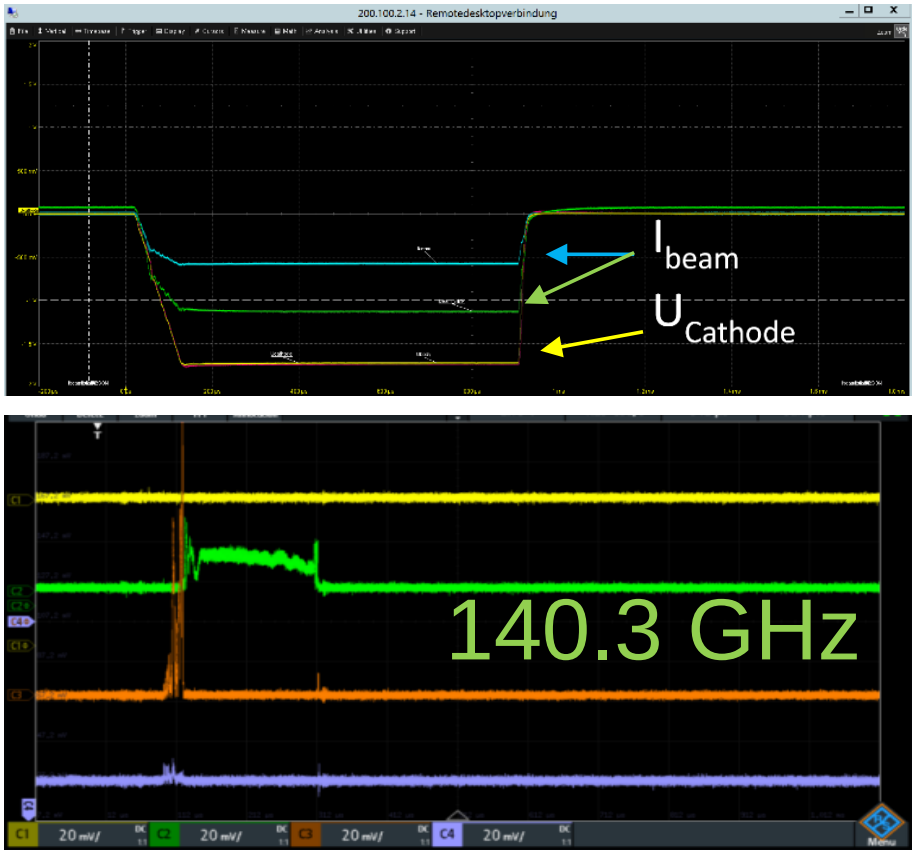

Fig. 1.3.3: Measurement of beam current and cathode voltage for ~ 1 ms pulse (top), first RF detection (filterbank signal) on FULGOR teststand (bottom).

1.4 Development of Multistage Depressed Collectors

Contact: M.Sc. Benjamin Ell

Multistage Depressed Collector (MDC) technology is one of the key components for high power continuous wave gyrotrons to significantly increase the overall tube efficiency. A target gyrotron efficiency of ≥ 60 % is planned for the compact *E*×*B* MDC prototype for the first short pulse experiments. The vacuum housing and the coils of the first MDC prototype were assembled at KIT in 2022 and are shown in Fig. 1.4.1 on the right, while a schematic of the MDC is shown on the left. Fabrication of the electrodes will start in the near future. At this stage, the collector is optimized for the KIT 170 GHz, 2 MW coaxial-cavity short-pulse gyrotron. However, the basic design of the electrodes can be used in several gyrotron configurations. To provide more flexibility for future experiments, a second, shorter version of the bottom section is fabricated to be compatible with the 140 GHz W7-X upgrade short-pulse gyrotron. A high collector efficiency of 75 % and a low reflected current were shown in the simulations.

Theoretical studies on other *E*×*B* drift collectors have been continued. These studies include, on the one hand, the continuous wave compatible design study carried out in recent years. On the other hand, for the first time, a novel collector sweeping system with electric fields is proposed. The presented mechanism is able to apply several orders higher sweeping frequencies to reduce the periodic variation of temperature compared to the traditional magnetic field sweeping systems with frequencies between 7-50 Hz. The *E*×*B* sweeping system is implemented at the inside of the gyrotron and is therefore not limited to such low frequencies due to eddy currents. Electrodes are placed at the entrance of the collector to generate an alternating azimuthal electric field for a sweeping of the electron beam in radial dimension.

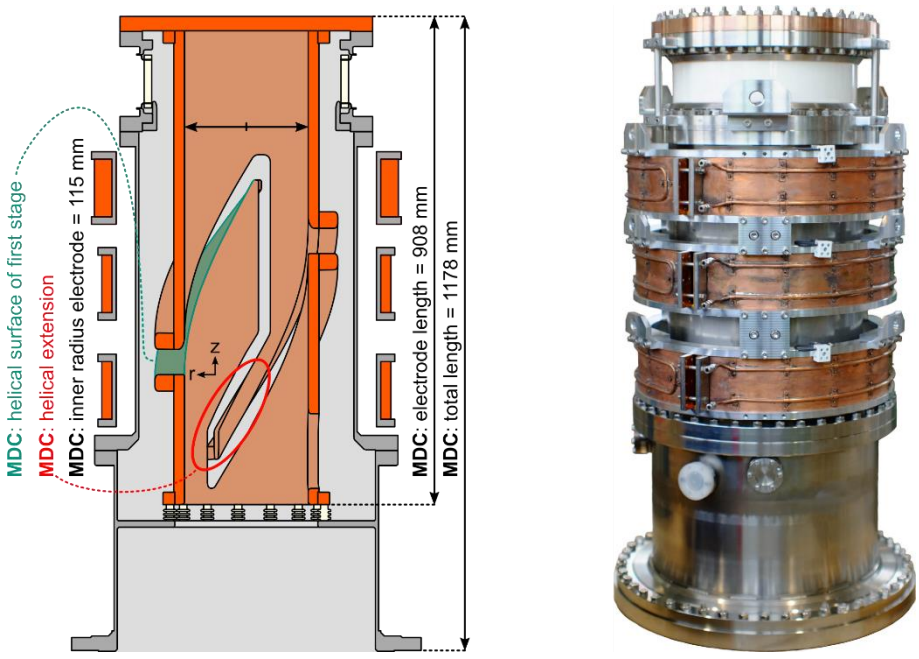

Fig. 1.4.1: Schematic view of the short pulse MDC prototype (left) and assembled prototype (right).

1.5 Quasi-optical mode converter, broadband window and Matching Optical Unit

Contact: Dr. Jianbo Jin

In 2022 work on the simulation of quasi-optical (QO) components for gyrotrons was focused on the following subjects.

1.5.1 A Quasi-Optical system and a Matching Optics Unit containing one quasi-quadratic mirror for a 117.5 GHz $TE_{24,8}$ mode gyrotron

A QO system has been designed to provide a RF beam with Gaussian mode content of 98.7% at the output window. An external Matching Optics Unit (MOU) contains one quasi-quadratic mirror has also been designed to transform the microwave beam to achieve a HE_{11}-mode content in the range of about 97.6 % to 98 % at the entry of the HE_{11} waveguide with I. D. = 31.75 mm.

1.5.2 Hybrid-type launcher for co- and counter-rotating modes

The method for the design of hybrid-type launchers has been developed for dual way hybrid-type launchers. The dual way launcher means that it can be used for a co-rotating mode $TE_{m,n}$ mode and also for a counter-rotating mode $TE_{-m,n}$ mode. As an example, a hybrid-type launcher for the $TE_{32,9}$ mode and for the $TE_{-32,9}$ mode at 170 GHz has been synthesized. The field distributions on the launcher wall are shown in Fig. 1.5.1, and the simulation results show that the Gaussian mode content of the microwave beam is 98.24 % at the launcher aperture.

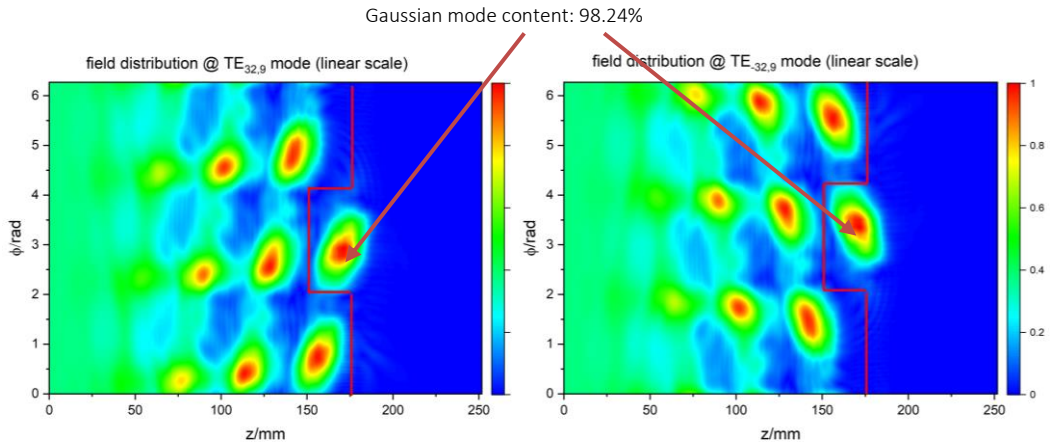

Fig. 1.5.1: Field distributions on the hybrid-type launcher wall and aperture: @$TE_{32,9}$ mode (left), $TE_{-32,9}$ mode (right).

1.5.3 Development of simulation tools to achieve a proper simulation of EM resonances in broadband windows

Some subroutines for the calculation of Magnetic Field Integral Equation (MFIE) have been developed and integrated into KARLESSS code. However, there are still some subroutines not been finished and the developed subroutines are still under debugging.

The in-house computer code ASRET for calculating the reflection of wave beams on window disk has been improved to account for variation of wavefront gradients of wave beams. The ASRET code has also been improved to analyze the reflection of high order Gaussian modes with the wavefront distribution included in the calculation. The reflection of Gaussian beams on Brewster-angle windows can also be calculated using the improved ASRET code with correct the wavefront distribution included. The simulation results show that the influence of the gradient deviation of wavefronts of Gaussian modes can be ignored on a typical high-power single disk gyrotron window, and the influence of the high order components could also be ignored. For a Brewster-angle window, the incidence angle is no longer a constant on the window surface. As an example, the reflection of an ideal Gausssian beam operating at 170 GHz on a Brewster-angle window has been calculated. Fig. 1.5.2 presents the distributions of the reflected power densities in the E- and H- planes. The reflected power on the Brewster-angle window is estimated to be $1x10^{-3}$ in the case that the beam waists are located on the window disk.

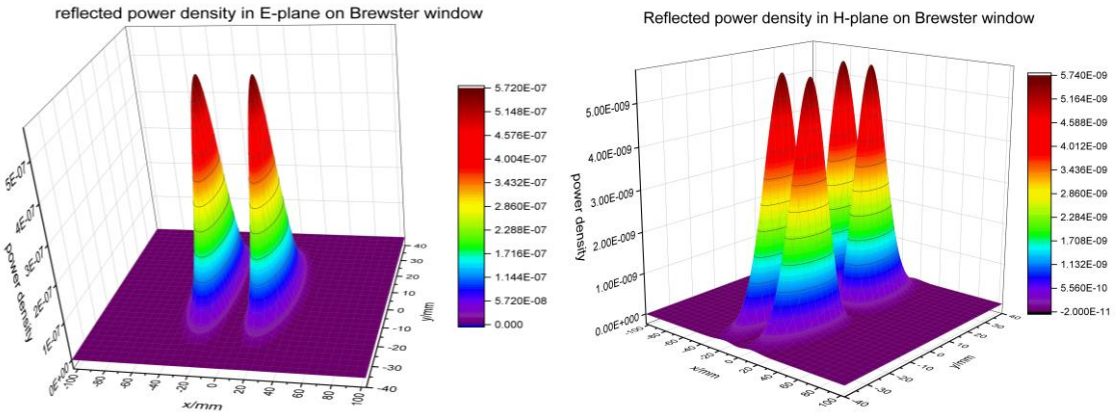

Fig. 1.5.2: Reflected power density of the linear polarized Gaussian beams in the E-plane (left) and H-plane (right) with gradient variation of wavefronts on the Brewsterangle window

1.5.4 A QO system and MOU operating at four frequencies

A new approach has been developed to improve the design of launchers for multi-center frequencies and broadband step-tunable gyrotrons. The approach can be described as follows.

$$f(\alpha, z) = \sum_i w_i f_i(\alpha, z) \quad (1)$$

Where $f(\alpha, z)$ describes the contour of the launcher wall, $f_i(\alpha, z)$ represents the contour of the launcher wall designed with respective to each center frequency, w_i is the weight, and (α, z) are the azimuthal and longitudinal coordinates defined in cylinder coordinate system. The weights should be optimized to supply relatively high conversion efficiency for all operating modes.

A QO system has been optimized for the conversion of four modes, for the $TE_{27,15}$ mode at 134 GHz, the $TE_{34,19}$ mode at 170 GHz, the $TE_{40,23}$ mode at 204 GHz and the $TE_{48,26}$ mode at 238 GHz. A MOU consisting of two quasi-quadratic mirrors has also been designed to transform the parameters of the Gaussian-like distributions output from the gyrotron to match the HE_{11} waveguide. The simulation results reveal that the HE_{11} mode contents of the RF beams are 96.5 % at 134 GHz, 98 % at 170 GHz. For the RF beams operating at 204 GHz and at 238 GHz, the HE_{11} mode contents are somewhat lower than the technical requirement (>95 %), so both the QO system and the MOU should be improved.

1.6 Frequency-Stabilization of W7-X Gyrotrons

Contact: M.Sc. Laurent Krier

The main tasks in 2022 were, firstly, the implementation of a frequency stabilization system for W7-X gyrotrons, and, secondly, the application of that system to Collective Thomson Scattering (CTS) diagnostics at Wendelstein 7-X stellarator.

Based on the previous work on a frequency stabilization system that uses a Phase-Locked Loop (PLL), a PLL system was implemented into a Field-Programmable-Gate-Array (FPGA). The implementation into the FPGA system allows for a simple adjustment of the control system, a flexible change of the operating parameters and an easy integration into the W7-X system.

The PLL system was applied to the CTS diagnostic system of W7-X. Target was an operation of CTS diagnostics at 174 GHz, knowing that the 140 GHz W7-X gyrotrons are not optimized for this frequency. An experimental campaign conducted during OP2. For the first time, one of the ECRH gyrotrons was operated at 174 GHz. Experiments with the PLL system were conducted to stabilize the gyrotron at 174 GHz. Main challenge was a stabilization at short pulses of 10 ms pulse length, konowing that the operating frequency of a gyrotron varies most at the start of the pulse. During the experiments, the gyrotron could be stabilized within 1.5 ms and be kept stable for the rest of the pulse. In Fig. 1.6.1, the frequency over time for the free-running and stabilized operation is shown.

Furthermore, theoretical investigations on a gyrotron with a triode-type MIG were conducted and the frequency dependence of the gyrotron on the modulation anode was investigated.

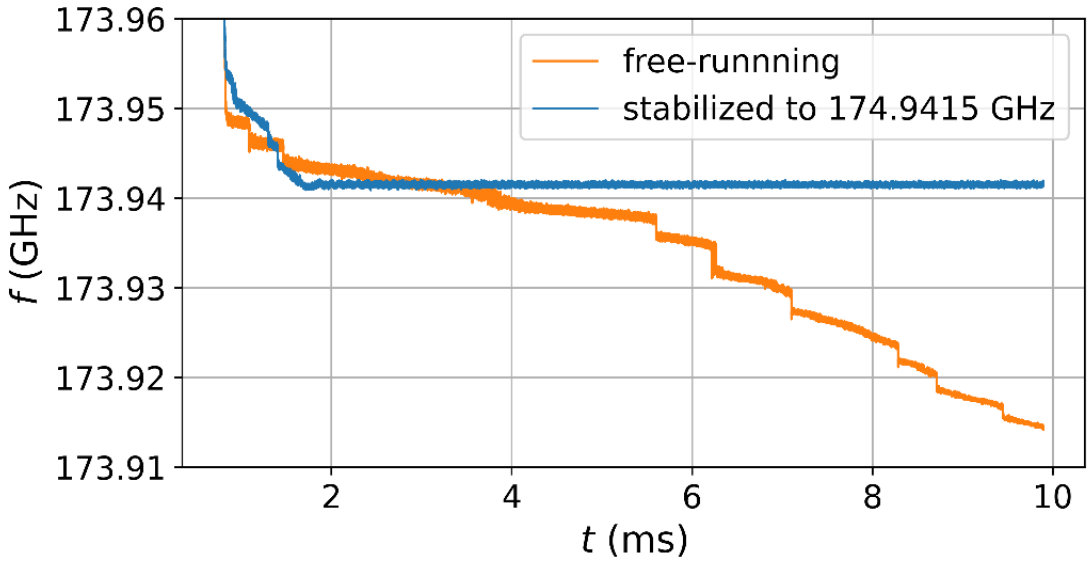

Fig. 1.6.1: Frequency over time for free-running and frequency stabilized operation

1.7 Plasma stabilization for DEMO

Contact: Dr.-Ing. Chuanren Wu

The IHM is par of the EUROfusion DEMO center design team. It is closely involved in the EC system design. To become more confident about the correct settings of the future EC system specification, the EUROfusion DEMO flight-simulator is used. Therefore, IHM is involved in the development of the flight simulator. It is done in close collaboration with IPP-Garching and, always, in frame of EUROfusion. One of the primary focuses during the year 2022 was to do a clean implementation of the connections between the physics calculations and the feedback control loops. The activities resulted in a new code module that can now be widely reused for different tokamaks and configurations. Furthermore, this new code enhances stability, maintainability and usability of the flight-simulator.

In collaboration with IPP-Garching, the simulation of the required heating power for entering H-mode in DEMO was reproduced. Utilizing a simplified model in the simulations a good agreement with the results from time-consuming models was achieved, depicted in the Fig. 1.7.1. The reproduced simulations provide more confidence in utilizing EC-only heating for the transition from L-mode to H-mode. In the next step, IHM will collaborate with IPP-Garching to revise the burn point and estimate the accessibility towards it through EC-only heating.

As part of the EUROfusion Work Package Heating and Current Drive, IHM worked together with other institutes to propose a modification to the port allocation scheme of DEMO. The new scheme is illustrated in the accompanying picture. The objective is to enhance the accessibility of all EC-ports from the gyrotron building(s), located on one side of the tokamak building. This new scheme has become the current common working assumption within EUROfusion.

Looking ahead to potential developments in 2023, a reduction of the aspect ratio of the DEMO tokamak is anticipated. Consequently, the new baseline configuration will likely require the use of ECCD (Electron Cyclotron Current Drive). We did a preliminary examination of the feasibility and performance of ECCD for the low-aspect DEMO. This analysis will serve as a foundation for future decisions and guide our ongoing research in this area.

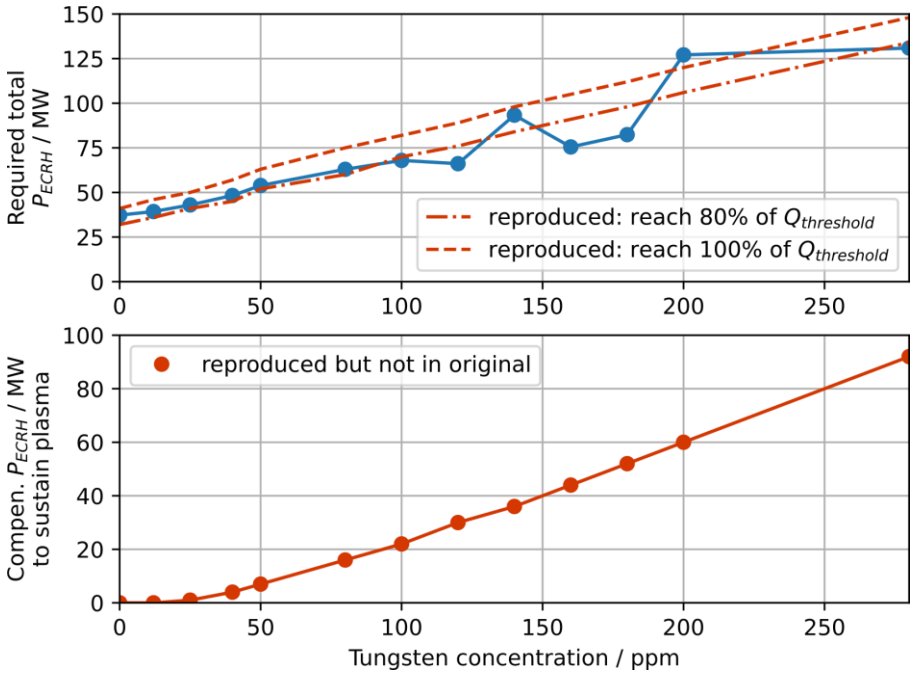

Fig. 1.7.1: Simulation of r equired heating power with varying concentrations of tungsten using a simplified transport model. (Blue dots represent results from time consuming simulations.)

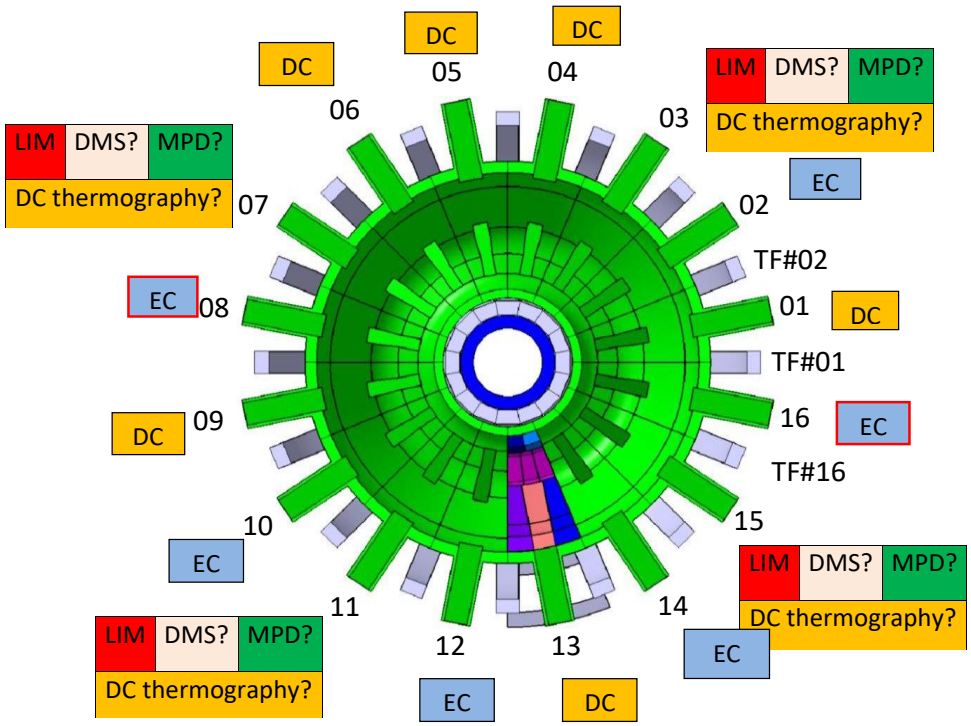

Fig. 1.7.2: Newly assumed port allocation scheme for facilitating access to tokamak ports by the EC system (DC: diagnostic and control. LIM: limiter, DMS: disruption mitigation system, MPD: multi-purpose deployer)

1.8 Design activities for a 105 GHz gyrotron

Contact: Dr. Gerd Gantenbein

The WEST tokamak, operated by CEA IRFM, Cadarache, France, aims at long pulse operation (~1000 s) in an ITER-like tungsten wall configuration. In order to ensure high performance operation of the plasma (H-mode) it has been decided to install a 3 MW 105 GHz ECRH system. The RF design of the 1 MW 105 GHz gyrotron has been performed by IHM in collaboration with the industrial manufacturer Thales, France. The design of the gyrotron is based on a 140 GHz 1.5 MW gyrotron with only small modifications.

A magnetron injection gun (MIG) has been designed, it shows a proper performance in terms of beam parameters and acceptable electric field strength at critical positions. The simulations show only a low risk of backreflected electrons.

According to numerical simulations on the interaction the mode $TE_{-20,8}$ has been selected as main operating mode. The operating parameters of the gyrotron are given in Table 1.8.1. The typical performance of the gyrotron during start-up and long-pulse operation due to multi-mode simulations are shown in Fig. 1.8.1. The $TE_{-20,8}$ mode will be transfered into a Gaussian beam with an optimised quasi-optical launcher antenna and focused with a 3-mirror system to the output window. With a test equipment the design of the launcher has been verified successfully in a low-power system. A comparison of the calculated and measured field shows a very good agreement (see Fig. 1.8.2).

The manufacturing and assembling of the tube at Thales will be finalised in 2023, first tests of this gyrotron at IHM are expected in second half of 2023.

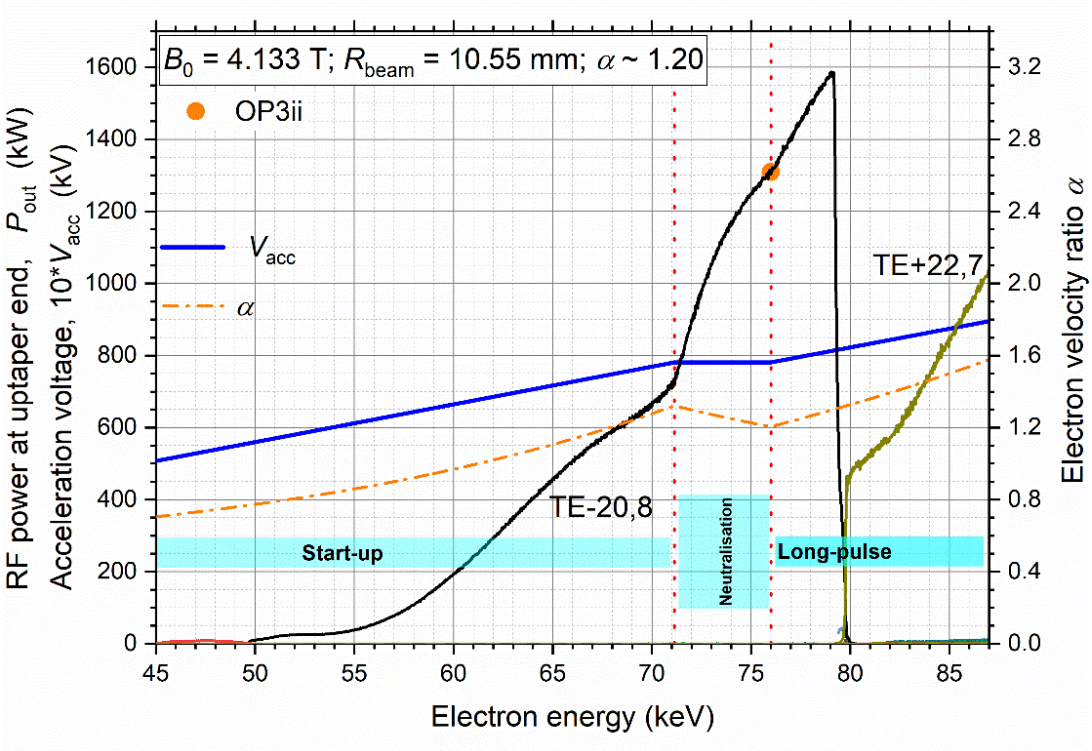

Fig. 1.8.1: Gyrotron performance during start-up and long-pulse operation.

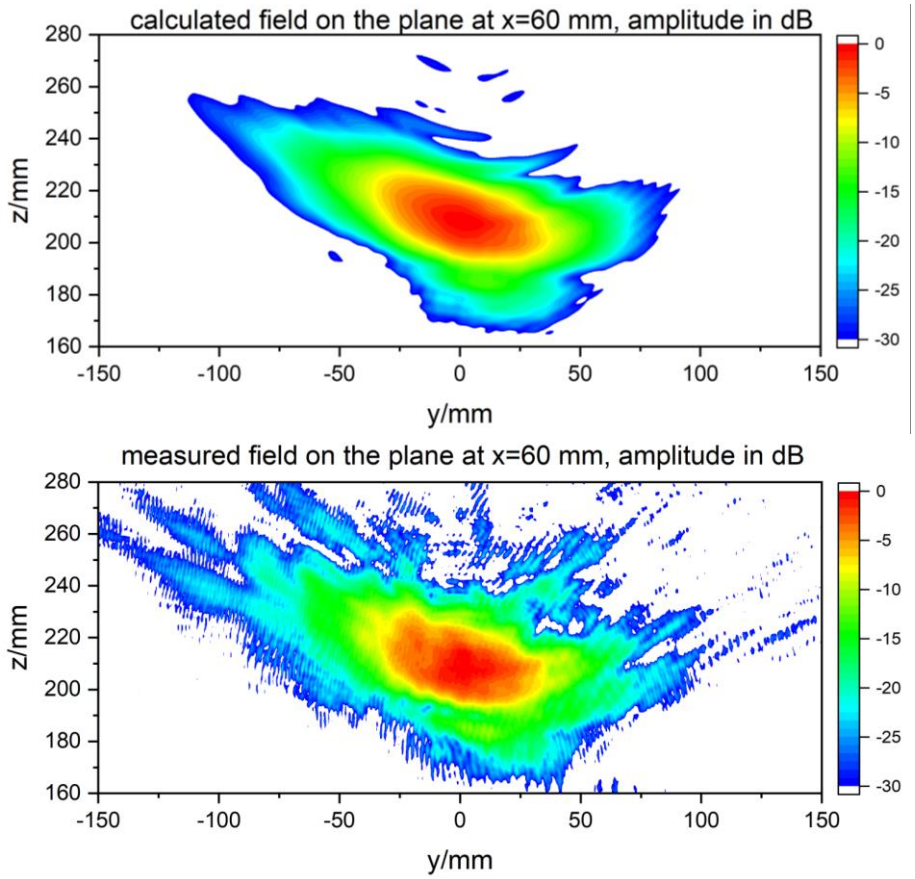

Fig. 1.8.2: Comparison of calculated RF field (top) and measurements (bottom)

Design Parameter	Value
Operating frequency	104.92 GHz
Operating cavity mode	$TE_{-20,8}$
Magnetic field	-4.13 T
Cathode voltage	-55 kV
Body Voltage	+23 kV
Accelerating voltage	78 kV
Beam current	45 A
RF power at cavity exit	1.30 MW
Gaussian mode content	98.85 %

Table 1.8.1: Operating parameters of a 105 GHz gyrotron

1.9 Broadband high-power amplifier system for 263 GHz DNP-NMR spectroscopy

Contact: M.Sc. Max Vöhringer

In recent years, dynamic nuclear polarization (DNP) magic angle spinning NMR has gained increasing interest because of a dramatic increase of SNR and therefore a substantial decrease of data sampling time up to a factor of 10^4. DNP is based on a polarization transfer from electrons to the nuclei of the atoms in the sample. This can be facilitated by a millimeter (mm)-wave, which frequency matches the resonant frequency of the electrons in the magnetic field of the NMR. To achieve the the desired power and frequency, high power oscillators (gyrotrons) are currently employed. Those devices use the relativistic electron cyclotron maser (ECM) interaction, but are not capable of producing coherent pulse sequences. However, to create such coherent pulse sequences, a new type of high-power amplifier system is needed.

The project B01 of the DFG Collaborative Research Center "Compact High Performance Magnetic Resonance Systems - HyPERiON (DFG SFB 1527) targets for such a high-power amplifier system. The final system shall provide an output power of 1 kW at a frequency of 263 GHz.

Figure 1.9.1 sketches the high-power amplifier system. It consists of three major parts.

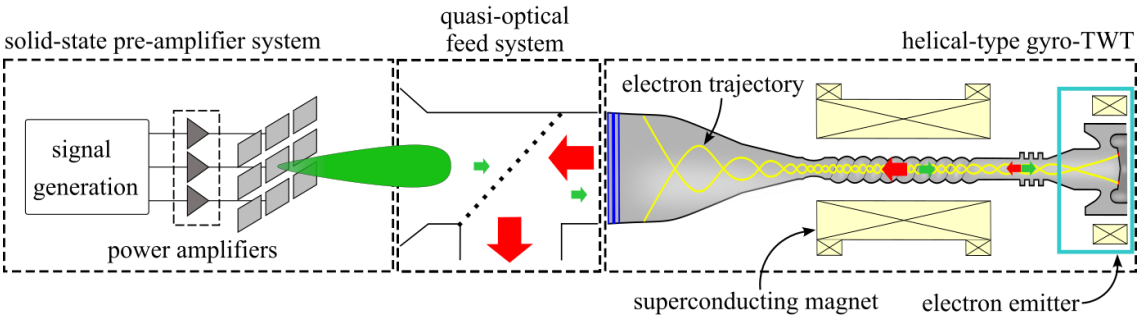

Fig. 1.9.1: Schematic of amplifier system. The signal power flow after the solid-state pre-amplifier is depicted in green, the power flow during and after amplification in the gyro-TWT is red.

First major part is a distributed solid-state upconverter and pre-amplifier system including an antenna array that radiates a linearily polarized beam (Fig. 1.9.1, left). The pre-amplifier system upconverts and amplifies the low power input signal to the final frequency of 263 GHz and to a level of a few hunded Milliwatts up to 1 Watt (Fig. 1.9.1, green arrows). The amplifier system is designed by the team of Prof. Cagri Ulusoy at the Institute of Radio Frequency Engineering and Electronics (IHE).

Second major part is a quasi-optical feed system. Major element of this quasi-optical feed system is a power splitter (Fig. 1.9.1, center). The power splitter directs the amplified signal coming from the solid-state pre-amplifier system towards the final high-power amplifier (Fig. 1.9.1, green arrows) whereas the output signal of the high-power amplifier is directed towards the DNP-NMR system (Fig. 1.9.1, red arrows).

Finally, a gyro-TWT with helically corrugated interaction region, the so-called helical gyro-TWT amplifies the signal to an output power of up to 1 kW. The helical-type gyro-TWT is an electron vacuum tube. The vacuum (Fig. 1.9.1, grey area) is required to sustain the high acceleration voltages in the emitter region (Fig. 1.9.1, violet), as well as to increase the mean free path of the electrons, so they are able to travel through the tube, without collisions with other particles (atoms, molecules). The free electrons are created

by the electron emitter, accelerated by an electric field and guided by the magnetic field of the superconducting magnet. This magnetic field also causes the electrons to gyrate. If the frequency of the gyrating electrons is similar to the frequency of the input signal, an energy transfer from electron beam to electromagnetic wave occurs. As a result, the signal is amplified. The spend electron beam is then collected by the collector and the remaining electron energy is dissipated as heat. The helical-type gyro-TWT is designed by IHM.

In a first step, the electron source and the superconducting magnet is designed. Both devices are most critical for the amplifier and are among the most expensive components of the tube. Additionally, the delivery time, especially for the superconducting magnet, is very long.

1.10 New concepts of sub-THz frequency-doubling amplifiers

Contact: Dr.-Ing. Alexander Marek

A new concept of frequency doubling gyrotron traveling wave amplifier (FD-GTWT) for applications that require high-power microwave in the sub-THz frequency range is developed. The proposed amplifier supports high power and high gain over a broad bandwidth and simultaneously doubles the frequency of the input signal.

Broadband high-power amplifiers at sub-THz frequencies are of interest for many scientific applications, e.g. future time-domain dynamic nuclear polarization (DNP) nuclear magnetic resonance (NMR) spectroscopy methods. While first prototypes have been successfully demonstrated, their development is still part of current research. A promising candidate for future broadband high-power sub-THz amplifiers are gyrotron traveling wave tubes with a helically corrugated waveguide (HCW) as interaction space. The helical gyrotron traveling-wave tubes (H-GTWTs) provide a broader bandwidth and can operate at lower magnetic fields because the electron-wave interaction takes place at the 2nd cyclotron harmonic.

However, the typical saturated gain of H-GTWTs is limited to 30 dB because of parasitic reflection-induced oscillations. This limitation can be solved by sectioning the interaction region into two short HCW parts, separated by a long below-cutoff drift region. Such a high-gain H-GTWT allows the usage of low-power drivers (10-100 mW), which are available at frequencies up to the W-band. However, generating 10 mW at sub-THz frequencies of 250 GHz or higher is still a challenge. Therefore, a modification of the high-gain H-GTWT concept is proposed, the FD-GTWT. While in a high-gain H-GTWT the bunching and amplification process (in the first and second HCW circuits) both occur at the 2nd harmonic, we propose the usage of an electron-wave interaction at the fundamental of the cyclotron harmonic for the bunching process. As a result, an input signal at the half frequency of the generated output signal is sufficient. This allows the use of available D-band solid-state amplifiers as driving RF sources for the generation of high-power RF signals at frequencies from 220-340 GHz.

In Fig. 1.10.1, simulation results (performed with CST Microwave Studio Suite) of a 263 GHz FD-GTWT are presented. The simulations show that for a 10 mW driving signal at 131.5 GHz an RF output power of 250 W at 263 GHz and a gain of >40 dB over a bandwidth of 17.5 GHz should be possible by the proposed novel amplifier concept.

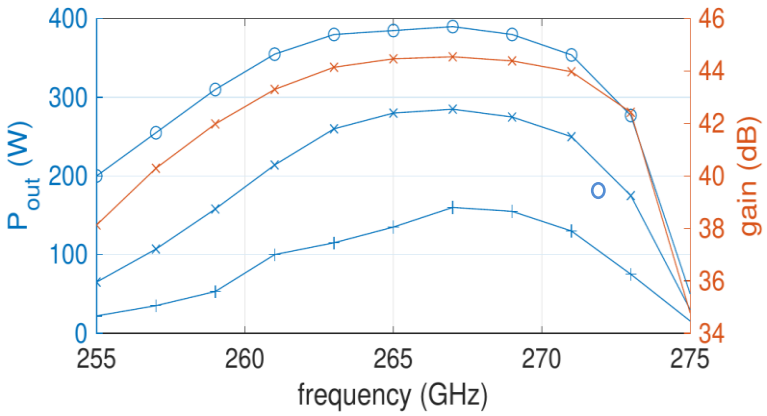

Fig. 1.10.1: Simulated output power versus the output frequency for an input signal at half the output frequency and different powers (= 30 mW; x = 10 mW; + = 5 mW). For a 10 mW input signal, the gain is given (red).

Journal Publications

W7-X Team; Szűcs, M.; Szepesi, T.; Biedermann, C.; Cseh, G.; Jakubowski, M.; Kocsis, G.; König, R.; Krause, M.; Sitjes, A. P.; Gantenbein, G.; Illy, S.; Jelonnek, J.; Krier, L.; Thumm, M. (2022). A Deep Learning-Based Method to Detect Hot-spots in the Visible Video Diagnostics of Wendelstein 7-X. Journal of Nuclear Engineering, 3 (4), 473–479. doi:10.3390/jne3040033

the W7-X Team; Andreeva, T.; Geiger, J.; Dinklage, A.; Wurden, G.; Thomsen, H.; Rahbarnia, K.; Schmitt, J. C.; Hirsch, M.; Fuchert, G.; Nührenberg, C.; Alonso, A.; Beidler, C. D.; Beurskens, M. N. A.; Bozhenkov, S.; Brakel, R.; Brandt, C.; Bykov, V.; Grahl, M.; Grulke, O.; Killer, C.; Kocsis, G.; Klinger, T.; Krämer-Flecken, A.; Lazerson, S.; Otte, M.; Pablant, N.; Schilling, J.; Windisch, T.; Gantenbein, G.; Huber, M.; Illy, S.; Jelonnek, J.; Kobarg, T.; Lang, R.; Leonhardt, W.; Mellein, D.; Papenfuß, D.; Thumm, M.; Wadle, S.; Weggen, J. (2022). Magnetic configuration scans during divertor operation of Wendelstein 7-X. Nuclear Fusion, 62 (2), Article no: 026032. doi:10.1088/1741-4326/ac3f1b

Wendelstein 7-X Team; Mencke, J. E.; Moseev, D.; Salewski, M.; Larsen, M. R.; Schmidt, B. S.; Järleblad, H.; Lazerson, S.; Poloskei, P. Z.; Ford, O.; Gantenbein, G.; Illy, S.; Jelonnek, J.; Krier, L.; Thumm, M. (2022). Characterization of correlations of fast-ion H-alpha measurement volumes in Wendelstein 7-X by particle tracking. Review of Scientific Instruments, 93 (12), Article no: 123503. doi:10.1063/5.0128594

Shcherbinin, V. I.; Tkachova, T. I.; Maksimenko, A. V.; Thumm, M.; Jelonnek, J. (2022). Novel Complex Cavity for Second-Harmonic Subterahertz Gyrotrons: a Tradeoff Between Engineering Tolerance and Mode Selection. Journal of Infrared, Millimeter, and Terahertz Waves, 43 (11-12), 957–971. doi:10.1007/s10762-022-00888-w

W7-X Team; Mayer, M.; Balden, M.; Brezinsek, S.; Burwitz, V. V.; Cupak, C.; Dhard, C. P.; Elgeti, S.; Corominas, M. G.; Hiret, P.; Kandler, M.; Naujoks, D.; Schmidt-Dencker, J.-H.; Ruset, C.; Saramela, T. B.; Silva, T. F.; Gantenbein, G.; Huber, M.; Illy, S.; Jelonnek, J.; Kobarg, T.; Lang, R.; Leonhardt, W.; Mellein, D.; Papenfuß, D.; Thumm, M.; Wadle, S.; Weggen, J. (2022). Carbon erosion/deposition on the divertor of W7-X during the operational period OP 1.2b. Nuclear Fusion, 62 (12), Article no: 126049. doi:10.1088/1741-4326/ac94e2

Wagner, D.; Kasparek, W.; Leuterer, F.; Monaco, F.; Ruess, T.; Schutz, H.; Stober, J.; Thumm, M. (2022). Compact Multi-Frequency Sub-THz Notch Filters with Rejection within and above the Pass Band. 2022 47th International Conference on Infrared, Millimeter and Terahertz Waves (IRMMW-THz), 2 S., Institute of Electrical and Electronics Engineers (IEEE). doi:10.1109/IRMMW-THz50927.2022.9895796

Miyazaki, A.; Lofnes, T.; Caspers, F.; Spagnolo, P.; Jelonnek, J.; Ruess, T.; Steinmann, J. L.; Thumm, M. (2022). Ultra narrowband detection scheme for dark photon / axion around 30 GHz. 47th International Conference on Infrared, Millimeter and Terahertz Waves (IRMMW-THz), 1 S., Institute of Electrical and Electronics Engineers (IEEE). doi:10.1109/IRMMW-THz50927.2022.9895788

W7-X Team; Zhao, M.; Masuzaki, S.; Motojima, G.; Tokitani, M.; Yajima, M.; Gao, Y.; Jakubowski, M.; Puig Sitjes, A.; Pisano, F.; Dhard, C. P.; Naujoks, D.; Romazanov, J.; Brezinsek, S.; Gantenbein, G.; Huber, M.; Illy, S.; Jelonnek, J.; Kobarg, T.; Lang, R.; Leonhardt, W.; Mellein, D.; Papenfuß, D.; Thumm, M.; Wadle, S.; Weggen, J. (2022). Distributions of deposits and hydrogen on the upper and lower TDUs3 target elements of Wendelstein 7-X. Nuclear Fusion, 62 (10), Article no: 106023. doi:10.1088/1741-4326/ac8c56

Swee, C.; Geiger, B.; Albosta, R.; Ford, O.; Loch, S.; Nornberg, M. D.; Schellpheffer, J.; Wegner, T.; Gantenbein, G.; Huber, M.; Illy, S.; Jelonnek, J.; Kobarg, T.; Lang, R.; Leonhardt, W.; Mellein, D.; Papenfuß, D.; Thumm, M.; Wadle, S.; Weggen, J.; Team, W.-X. (2022). Design of a new charge exchange recombination spectroscopy diagnostic for impurity transport experiments at Wendelstein 7-X. Review of Scientific Instruments, 93 (10), 103523. doi:10.1063/5.0101842

Goodman, T. P.; Alberti, S.; Genoud, J.; Torreblanca, H.; Albajar, F.; Sanchez, F.; Leggieri, A.; Legrand, F.; Lievin, C.; Ioannidis, Z.; Avramidis, K. A.; Tigelis, I.; Illy, S.; Hogge, J.-P. (2022). Tests and Qualification of the European 1 MW, 170 GHz CW Gyrotron in an ITER relevant configuration at SPC. 2022 47th International Conference on Infrared, Millimeter and Terahertz Waves (IRMMW-THz), 1–2, Institute of Electrical and Electronics Engineers (IEEE). doi:10.1109/IRMMW-THz50927.2022.9895782

Rzesnicki, T.; Avramidis, K. A.; Chelis, I.; Gantenbein, G.; Illy, S.; Ioannidis, Z. C.; Jin, J.; Thumm, M.; Jelonnek, J. (2022). 1.5 MW, 140 GHz Gyrotron for W7-X - development status and experimental results -. 2022 47th International Conference on Infrared, Millimeter and Terahertz Waves (IRMMW-THz), 1–2, Institute of Electrical and Electronics Engineers (IEEE). doi:10.1109/IRMMW-THz50927.2022.9896025

Vöhringer, M.; Marek, A.; Illy, S.; Gantenbein, G.; Thumm, M.; Wu, C.; Jelonnek, J. (2022). Development of a CUSP-Type Electron Gun for a W-Band Helical Gyro-TWT. 2022 47th International Conference on Infrared, Millimeter and Terahertz Waves (IRMMW-THz), 1–2, Institute of Electrical and Electronics Engineers (IEEE). doi:10.1109/IRMMW-THz50927.2022.9895903

Jin, J.; Gantenbein, G.; Illy, S.; Jelonnek, J.; Thumm, M. (2022). Progress of the Methods for Optimum of Quasi-Optical Mode Converters at KIT. 47th International Conference on Infrared, Millimeter and Terahertz Waves (IRMMW-THz), Delft, 28.th August - 2nd September 2022, 1–2, Institute of Electrical and Electronics Engineers (IEEE). doi:10.1109/IRMMW-THz50927.2022.9895682

Rzesnicki, T.; Albajar, F.; Avramidis, K. A.; Chelis, I.; Gantenbein, G.; Hogge, J.-P.; Illy, S.; Ioannidis, Z. C.; Jelonnek, J.; Jin, J.; Leggieri, A.; Legrand, F.; Pagonakis, I. G.; Sanchez, F.; Thumm, M. (2022). European 1 MW, 170 GHz CW Gyrotron Prototype for ITER - long-pulse operation at KIT -. 2022 47th International Conference on Infrared, Millimeter and Terahertz Waves (IRMMW-THz), 1–2, Institute of Electrical and Electronics Engineers (IEEE). doi:10.1109/IRMMW-THz50927.2022.9896073

Gantenbein, G.; Illy, S.; Jelonnek, J.; Ruess, T.; Rzesnicki, T.; Schmid, M.; Stanculovic, S. (2022). Status and First Operation of Gyrotron Teststand FULGOR at KIT. 2022 47th International Conference on Infrared, Millimeter and Terahertz Waves (IRMMW-THz), 1–2, Institute of Electrical and Electronics Engineers (IEEE). doi:10.1109/IRMMW-THz50927.2022.9895889

Marek, A.; Feuerstein, L.; Illy, S.; Thumm, M.; Wu, C.; Jelonnek, J. (2022). New Type of Pulsed High-Power sub-THz Source Based on Helical-Type Gyro-TWTs. 47th International Conference on Infrared, Millimeter and Terahertz Waves (IRMMW-THz), Delft, 28th August - 2nd September 2022, 1–4, Institute of Electrical and Electronics Engineers (IEEE). doi:10.1109/IRMMW-THz50927.2022.9895769

Bold, D.; Reimold, F.; Niemann, H.; Gao, Y.; Jakubowski, M.; Killer, C.; Winters, V. R.; Gantenbein, G.; Huber, M.; Illy, S.; Jelonnek, J.; Kobarg, T.; Lang, R.; Leonhardt, W.; Mellein, D.; Papenfuß, D.; Thumm, M.; Wadle, S.; Weggen, J.; W7-X Team. (2022). Parametrisation of target heat flux distribution and study of transport parameters for boundary modelling in W7-X. Nuclear Fusion, 62 (10), Artikel-Nr.: 106011. doi:10.1088/1741-4326/ac7e2f

Zhou, S.; Liang, Y.; Knieps, A.; Suzuki, Y.; Geiger, J.; Dinklage, A.; Langenberg, A.; Pasch, E.; Jakubowski, M.; Pablant, N.; Wang, N. C.; Drews, P.; Bozhenkov, S.; Liu, S.; Xu, S.; Gao, Y.; Ding, Y. H.; Huang, Z.; W7-X Team; Gantenbein, G.; Huber, M.; Illy, S.; Jelonnek, J.; Kobarg, T.; Lang, R.; Leonhardt, W.; Mellein, D.; Papenfuß, D.; Thumm, M.; Wadle, S.; Weggen, J. (2022). Equilibrium effects on the structure of island divertor and its impact on the divertor heat flux distribution in Wendelstein 7-X. Nuclear Fusion, 62 (10), Artikel-Nr.: 106002. doi:10.1088/1741-4326/ac8439

Alonso, J. A.; Ford, O. P.; Vanó, L.; Äkäslompolo, S.; Buller, S.; McDermott, R.; Smith, H. M.; Baldzuhn, J.; Beidler, C. D.; Beurskens, M.; Bozhenkov, S.; Brunner, K. J.; Calvo, I.; Carralero, D.; Dinklage, A.; Estrada, T.; Fuchert, G.; Geiger, J.; Knauer, J.; Langenberg, A.; Pablant, N. A.; Pasch, E.; Poloskei, P. Z.; Velasco, J. L.; Windisch, T.; the W7-X Team; Gantenbein, G.; Huber, M.; Illy, S.; Jelonnek, J.; Kobarg, T.; Lang, R.; Leonhardt, W.; Mellein, D.; Papenfuß, D.; Thumm, M.; Wadle, S.; Weggen, J. (2022). Plasma flow

measurements based on charge exchange recombination spectroscopy in the Wendelstein 7-X stellarator. Nuclear Fusion, 62 (10), Artikel-Nr.: 106005. doi:10.1088/1741-4326/ac7e5b

Wenzel, U.; Schlisio, G.; Drewelow, P.; Krychowiak, M.; König, R.; Pedersen, T. S.; Bozhenkov, S.; Haak, V.; Kharwandikar, A. K.; Lazerson, S.; Naujoks, D.; Perseo, V.; Winters, V.; the W7-X Team; Gantenbein, G.; Huber, M.; Illy, S.; Jelonnek, J.; Kobarg, T.; Lang, R.; Leonhardt, W.; Mellein, D.; Papenfuß, D.; Thumm, M.; Wadle, S.; Weggen, J. (2022). Gas exhaust in the Wendelstein 7-X stellarator during the first divertor operation. Nuclear Fusion, 62 (9), Art.-Nr.: 096016. doi:10.1088/1741-4326/ac7ac4

Li, Y.; Xu, G.; Dudson, B.; Liu, X.; Huang, Z.; Killer, C.; Feng, Y.; Liu, S.; Yan, N.; Morales, J.; Tsitrone, E.; Brezinsek, S.; Liang, Y.; Eldon, D.; Xiao, C.; Geiger, J.; Grulke, O.; Otte, M.; the WEST Team; the W7-X Team; Gantenbein, G.; Huber, M.; Illy, S.; Jelonnek, J.; Kobarg, T.; Lang, R.; Leonhardt, W.; Mellein, D.; Papenfuß, D.; Thumm, M.; Wadle, S.; Weggen, J. (2022). Effect of magnetic geometry on the energy partition between ions and electrons in the scrape-off layer of magnetic fusion devices. Nuclear Fusion, 62 (9), Art.Nr.: 094002. doi:10.1088/1741-4326/ac7df1

Marek, A.; Avramidis, K. A.; Feuerstein, L.; Illy, S.; Thumm, M.; Wu, C.; Jelonnek, J. (2022). Time-Domain Simulation of Helical Gyro-TWTs With Coupled Modes Method and 3-D Particle Beam. IEEE Transactions on Electron Devices, 69 (8), 4546–4552. doi:10.1109/TED.2022.3182292

Marek, A.; Feuerstein, L.; Illy, S.; Thumm, M.; Wu, C.; Jelonnek, J. (2022). New Type of sub-THz Frequency-Doubling Gyro-TWT with Helically Corrugated Circuit. IEEE Electron Device Letters, 43 (8), 1347–1350. doi:10.1109/LED.2022.3185288

Tran, M. Q.; Agostinetti, P.; Aiello, G.; Avramidis, K.; Baiocchi, B.; Barbisan, M.; Bobkov, V.; Briefi, S.; Bruschi, A.; Chavan, R.; Chelis, I.; Day, C.; Delogu, R.; Ell, B.; Fanale, F.; Fassina, A.; Fantz, U.; Faugel, H.; Figini, L.; Fiorucci, D.; Friedl, R.; Franke, T.; Gantenbein, G.; Garavaglia, S.; Granucci, G.; Hanke, S.; Hogge, J.-P.; Hopf, C.; Kostic, A.; Illy, S.; Ioannidis, Z.; Jelonnek, J.; Jin, J.; Latsas, G.; Louche, F.; Maquet, V.; Maggiora, R.; Messiaen, A.; Milanesio, D.; Mimo, A.; Moro, A.; Ochoukov, R.; Ongena, J.; Pagonakis, I. G.; Peponis, D.; Pimazzoni, A.; Ragona, R.; Rispoli, N.; Ruess, T.; Rzesnicki, T.; Scherer, T.; Spaeh, P.; Starnella, G.; Strauss, D.; Thumm, M.; Tierens, W.; Tigelis, I.; Tsironis, C.; Usoltceva, M.; Van Eester, D.; Veronese, F.; Vincenzi, P.; Wagner, F.; Wu, C.; Zeus, F.; Zhang, W. (2022). Status and future development of Heating and Current Drive for the EU DEMO. Fusion Engineering and Design, 180, Article no: 113159. doi.org/10.1016/j.fusengdes.2022.113159

Feuerstein, L.; Marek, A.; Avramidis, K. A.; Illy, S.; Wu, C.; Jelonnek, J. (2022). Validation of a New Fast-Time Scale Code for Advanced Simulations of Gyrotron Cavities. 14th German Microwave Conference (GeMiC), Ulm, 16-18 May 2022, 144–147, Institute of Electrical and Electronics Engineers (IEEE).

Ruess, T.; Gantenbein, G.; Jin, J.; Marek, A.; Rzesnicki, T.; Thumm, M.; Wagner, D.; Jelonnek, J. (2022). Verification of the 170/204 GHz Quasi-Optical Output Coupler of the 2 MW Coaxial-Cavity Gyrotron using a Mode Generator Setup. 2022 14th German Microwave Conference (GeMiC), Ulm, 16-18 May 2022, 5–8, Institute of Electrical and Electronics Engineers (IEEE).

Knieps, A.; Liang, Y.; Drews, P.; Endler, M.; Gao, Y.; Geiger, J.; Jakubowski, M.; Koenig, R.; Niemann, H.; Wang, F. Q.; Xu, S.; Zhou, S.; Gantenbein, G.; Huber, M.; Illy, S.; Jelonnek, J.; Kobarg, T.; Lang, R.; Leonhardt, W.; Mellein, D.; Papenfuß, D.; Thumm, M.; Wadle, S.; Weggen, J. (2022). Anisotropic diffusion as a proxy model for the estimation of heat-loads on plasma-facing components. Plasma Physics and Controlled Fusion, 64 (8), Article no: 084001. doi:10.1088/1361-6587/ac757d

Leggieri, A.; Bariou, D.; Hermann, V.; Legrand, F.; Lietaer, G.; Lievin, C.; Marchesin, R.; Thouvenin, P.; Albajar, F.; Sanchez, F.; Avramidis, K. A.; Gantenbein, G.; Illy, S.; Ioannidis, Z.; Jelonnek, J.; Jin, J.; Pagonakis, I. G.; Rzesnicki, T.; Thumm, M.; Alberti, S.; Hogge, J.-P.; Allio, A.; Difonzo, R.; Savoldi, L.; Chelis, I.; Tigelis, I.; Latsas, G.; Bin, W.; Bruschi, A.; Fanale, F. (2022). TH1509U European 170 GHZ 1 MW CW Industrial Gyrotron

Upgrade. 2021 22nd International Vacuum Electronics Conference (IVEC), 1–2, Institute of Electrical and Electronics Engineers (IEEE). doi:10.1109/IVEC51707.2021.9722467

Sunn Pedersen, T.; Abramovic, I.; Agostinetti, P.; Agredano Torres, M.; Äkäslompolo, S.; Alcuson Belloso, J.; Aleynikov, P.; Aleynikova, K.; Alhashimi, M.; Ali, A.; Allen, N.; Alonso, A.; Anda, G.; Andreeva, T.; Angioni, C.; Arkhipov, A.; Arnold, A.; Asad, W.; Ascasibar, E.; Aumeunier, M.-H.; Avramidis, K.; Aymerich, E.; Baek, S.-G.; Bähner, J.; Baillod, A.; Balden, M.; Balden, M.; Baldzuhn, J.; Ballinger, S.; Banduch, M.; Bannmann, S.; Banon Navarro, A.; Bañón Navarro, A.; Barbui, T.; Beidler, C.; Belafdil, C.; Bencze, A.; Benndorf, A.; Beurskens, M.; Biedermann, C.; Biletskyi, O.; Blackwell, B.; Blatzheim, M.; Bluhm, T.; Böckenhoff, D.; Bongiovi, G.; Borchardt, M.; Borodin, D.; Boscary, J.; Bosch, H.; Bosmann, T.; Böswirth, B.; Böttger, L.; Bottino, A.; Bozhenkov, S.; Brakel, R.; Brandt, C.; Bräuer, T.; Braune, H.; Brezinsek, S.; Brunner, K.; Buller, S.; Burhenn, R.; Bussiahn, R.; Buttenschön, B.; Buzás, A.; Bykov, V.; Calvo, I.; Camacho Mata, K.; Caminal, I.; Cannas, B.; Cappa, A.; Carls, A.; Carovani, F.; Carr, M.; Carralero, D.; Carvalho, B.; Casas, J.; Castano-Bardawil, D.; Castejon, F.; Chaudhary, N.; Chelis, I.; Chomiczewska, A.; Coenen, J. W.; Cole, M.; Cordella, F.; Corre, Y.; Crombe, K.; Cseh, G.; Csillag, B.; Damm, H.; Day, C.; de Baar, M.; De la Cal, E.; Degenkolbe, S.; Demby, A.; Denk, S.; Dhard, C.; Di Siena, A.; Dinklage, A.; Dittmar, T.; Dreval, M.; Drevlak, M.; Drewelow, P.; Drews, P.; Dunai, D.; Edlund, E.; Effenberg, F.; Ehrke, G.; Endler, M.; Ennis, D. A.; Escoto, F. J.; Estrada, T.; Fable, E.; Fahrenkamp, N.; Fanni, A.; Faustin, J.; Fellinger, J.; Feng, Y.; Figacz, W.; Flom, E.; Ford, O.; Fornal, T.; Frerichs, H.; Freundt, S.; Fuchert, G.; Fukuyama, M.; Füllenbach, F.; Gantenbein, G.; Gao, Y.; Garcia, K.; García Regaña, J. M.; García-Cortés, I.; Gaspar, J.; Gates, D. A.; Geiger, J.; Geiger, B.; Giudicotti, L.; González, A.; Goriaev, A.; Gradic, D.; Grahl, M.; Graves, J. P.; Green, J.; Grelier, E.; Greuner, H.; Groß, S.; Grote, H.; Groth, M.; Gruca, M.; Grulke, O.; Grün, M.; Guerrero Arnaiz, J.; Günter, S.; Haak, V.; Haas, M.; Hacker, P.; Hakola, A.; Hallenbert, A.; Hammond, K.; Han, X.; Hansen, S. K.; Harris, J. H.; Hartfuß, H.; Hartmann, D.; Hathiramani, D.; Hatzky, R.; Hawke, J.; Hegedus, S.; Hein, B.; Heinemann, B.; Helander, P.; Henneberg, S.; Hergenhahn, U.; Hidalgo, C.; Hindenlang, F.; Hirsch, M.; Höfel, U.; Hollfeld, K. P.; Holtz, A.; Hopf, D.; Höschen, D.; Houry, M.; Howard, J.; Huang, X.; Hubeny, M.; Hudson, S.; Ida, K.; Igitkhanov, Y.; Igochine, V.; Illy, S.; Ionita-Schrittwieser, C.; Isobe, M.; Jabłczyńska, M.; Jablonski, S.; Jagielski, B.; Jakubowski, M.; Jansen van Vuuren, A.; Jelonnek, J.; Jenko, F.; Jenko, F.; Jensen, T.; Jenzsch, H.; Junghanns, P.; Kaczmarczyk, J.; Kallmeyer, J.; Kamionka, U.; Kandler, M.; Kasilov, S.; Kazakov, Y.; Kennedy, D.; Kharwandikar, A.; Khokhlov, M.; Kiefer, C.; Killer, C.; Kirschner, A.; Kleiber, R.; Klinger, T.; Klose, S.; Knauer, J.; Knieps, A.; Köchl, F.; Kocsis, G.; Kolesnichenko, Y. I.; Könies, A.; König, R.; Kontula, J.; Kornejew, P.; Koschinsky, J.; Kozulia, M. M.; Krämer-Flecken, A.; Krampitz, R.; Krause, M.; Krawczyk, N.; Kremeyer, T.; Krier, L.; Kriete, D. M.; Krychowiak, M.; Ksiazek, I.; Kubkowska, M.; Kuczynski, M.; Kühner, G.; Kumar, A.; Kurki-Suonio, T.; Kwak, S.; Landreman, M.; Lang, P. T.; Langenberg, A.; Laqua, H. P.; Laqua, H.; Laube, R.; Lazerson, S.; Lewerentz, M.; Li, C.; Liang, Y.; Linsmeier, C.; Lion, J.; Litnovsky, A.; Liu, S.; Lobsien, J.; Loizu, J.; Lore, J.; Lorenz, A.; Losada, U.; Louche, F.; Lunsford, R.; Lutsenko, V.; Machielsen, M.; Mackel, F.; Maisano-Brown, J.; Maj, O.; Makowski, D.; Manduchi, G.; Maragkoudakis, E.; Marchuk, O.; Marsen, S.; Martines, E.; Martinez-Fernandez, J.; Marushchenko, M.; Masuzaki, S.; Maurer, D.; Mayer, M.; McCarthy, K. J.; Mccormack, O.; McNeely, P.; Meister, H.; Mendelevitch, B.; Mendes, S.; Merlo, A.; Messian, A.; Mielczarek, A.; Mishchenko, O.; Missal, B.; Mitteau, R.; Moiseenko, V. E.; Mollen, A.; Moncada, V.; Mönnich, T.; Morisaki, T.; Moseev, D.; Motojima, G.; Mulas, S.; Mulsow, M.; Nagel, M.; Naujoks, D.; Naulin, V.; Neelis, T.; Neilson, H.; Neu, R.; Neubauer, O.; Neuner, U.; Nicolai, D.; Nielsen, S. K.; Niemann, H.; Nishiza, T.; Nishizawa, T.; Nishizawa, T.; Nührenberg, C.; Ochoukov, R.; Oelmann, J.; Offermanns, G.; Ogawa, K.; Okamura, S.; Ölmanns, J.; Ongena, J.; Oosterbeek, J.; Otte, M.; Pablant, N.; Panadero Alvarez, N.; Panadero Alvarez, N.; Pandey, A.; Pasch, E.; Pavlichenko, R.; Pavone, A.; Pawelec, E.; Pechstein, G.; Pelka, G.; Perseo, V.; Peterson, B.; Pilopp, D.; Pingel, S.; Pisano, F.; Plöckl, B.; Plunk, G.; Pölöskei, P.; Pompe, B.; Popov, A.; Porkolab, M.; Proll, J.; Pueschel, M. J.; Puiatti, M.-E.; Puig Sitjes, A.; Purps, F.; Rahbarnia, K.; Rasiński, M.; Rasmussen, J.; Reiman, A.; Reimold, F.; Reisner, M.; Reiter, D.; Richou, M.; Riedl, R.; Riemann, J.; Rißе, K.; Roberg-Clark, G.; Rohde, V.; Romazanov, J.; Rondeshagen, D.; Rong, P.; Rudischhauser, L.; Rummel, T.; Rummel, K.; Runov, A.; Rust, N.; Ryc, L.; Salembier, P.; Salewski, M.; Sanchez, E.; Satake, S.; Satheeswaran, G.; Schacht, J.; Scharff, E.; Schauer, F.; Schilling, J.; Schlisio, G.; Schmid, K.; Schmitt, J.; Schmitz, O.; Schneider, W.; Schneider, M.; Schneider, P.; Schrittwieser, R.; Schröder, T.; Schröder, M.; Schroeder, R.; Schweer, B.; Schwörer, D.; Scott, E.; Scott, E.; Shanahan, B.; Sias, G.; Sichta, P.; Singer, M.; Sinha, P.; Sipliä, S.; Slaby, C.; Sleczka, M.; Smith, H.; Smoniewski, J.; Sonnendrücker, E.; Spolaore, M.; Spring, A.; Stadler, R.; Stańczak, D.; Stange, T.; Stepanov, I.; Stephey, L.; Stober, J.; Stroth, U.;

Strumberger, E.; Suzuki, C.; Suzuki, Y.; Svensson, J.; Szabolics, T.; Szepesi, T.; Szücs, M.; Tabarés, F. L.; Tamura, N.; Tancetti, A.; Tantos, C.; Terry, J.; Thienpondt, H.; Thomsen, H.; Thumm, M.; Travere, J. M.; Traverso, P.; Tretter, J.; Trier, E.; Trimino Mora, H.; Tsujimura, T.; Turkin, Y.; Tykhyi, A.; Unterberg, B.; van Eeten, P.; van Milligen, B. P.; van Schoor, M.; Vano, L.; Varoutis, S.; Vecsei, M.; Vela, L.; Velasco, J. L.; Vervier, M.; Vianello, N.; Viebke, H.; Vilbrandt, R.; Vogel, G.; Vogt, N.; Volkhausen, C.; von Stechow, A.; Wagner, F.; Wang, E.; Wang, H.; Warmer, F.; Wauters, T.; Wegener, L.; Wegner, T.; Weir, G.; Wenzel, U.; White, A.; Wilde, F.; Wilms, F.; Windisch, T.; Winkler, M.; Winter, A.; Winters, V.; Wolf, R.; Wright, A. M.; Wurden, G. A.; Xanthopoulos, P.; Xu, S.; Yamada, H.; Yamaguchi, H.; Yokoyama, M.; Yoshinuma, M.; Yu, Q.; Zamanov, M.; Zanini, M.; Zarnstorff, M.; Zhang, D.; Zhou, S.; Zhu, J.; Zhu, C.; Zilker, M.; Zocco, A.; Zohm, H.; Zoletnik, S.; Zsuga, L. (2022). Experimental confirmation of efficient island divertor operation and successful neoclassical transport optimization in Wendelstein 7-X. Nuclear Fusion, 62 (4), Article no: 042022. doi:10.1088/1741-4326/ac2cf5

Gradic, D.; Krychowiak, M.; König, R.; Henke, F.; Otte, M.; Perseo, V.; Pedersen, T. S.; W7-X Team; Gantenbein, G.; Huber, M.; Illy, S.; Jelonnek, J.; Kobarg, T.; Lang, R.; Leonhardt, W.; Mellein, D.; Papenfuß, D.; Thumm, M.; Wadle, S.; Weggen, J. (2022). Impurity temperatures measured via line shape analysis in the island scrape-off-layer of Wendelstein 7-X. Plasma Physics and Controlled Fusion, 64 (7), Art.-Nr.: 075010. doi:10.1088/1361-6587/ac70fa

Kremeyer, T.; König, R.; Brezinsek, S.; Schmitz, O.; Feng, Y.; Winters, V.; Rudischhauser, L.; Buttenschön, B.; Brunner, K. J.; Drewelow, P.; Flom, E.; Fuchert, G.; Gao, Y.; Geiger, J.; Jakubowski, M.; Killer, C.; Knauer, J.; Krychowiak, M.; Lazerson, S.; Reimold, F.; Schlisio, G.; Viebke, H.; the W7-X Team; Gantenbein, G.; Huber, M.; Illy, S.; Jelonnek, J.; Kobarg, T.; Lang, R.; Leonhardt, W.; Mellein, D.; Papenfuß, D.; Thumm, M.; Wadle, S.; Weggen, J. (2022). Analysis of hydrogen fueling, recycling, and confinement at Wendelstein 7-X via a single-reservoir particle balance. Nuclear Fusion, 62 (3), Art.-Nr.: 036023. doi:10.1088/1741-4326/ac4acb

Chaudhary, N.; Hirsch, M.; Hoefel, U.; Oosterbeek, J. W.; Marushchenko, N. B.; Wolf, R. C.; Gantenbein, G.; Huber, M.; Illy, S.; Jelonnek, J.; Kobarg, T.; Lang, R.; Leonhardt, W.; Mellein, D.; Papenfuß, D.; Thumm, M.; Wadle, S.; Weggen, J.; W7-X Team. (2022). Electron temperature profile from optically grey X3-mode of electron cyclotron emission at Wendelstein 7-X using Bayesian analysis. Plasma Physics and Controlled Fusion, 64 (5), 055016. doi:10.1088/1361-6587/ac5df3

Tancetti, A.; Nielsen, S. K.; Rasmussen, J.; Gusakov, E. Z.; Popov, A. Y.; Moseev, D.; Stange, T.; Senstius, M. G.; Killer, C.; Vecséi, M.; Jensen, T.; Zanini, M.; Abramovic, I.; Stejner, M.; Anda, G.; Dunai, D.; Zoletnik, S.; Laqua, H. P.; the W7-X Team; Gantenbein, G.; Huber, M.; Illy, S.; Jelonnek, J.; Kobarg, T.; Lang, R.; Leonhardt, W.; Mellein, D.; Papenfuß, D.; Thumm, M.; Wadle, S.; Weggen, J. (2022). Nonlinear decay of high-power microwaves into trapped modes in inhomogeneous plasma. Nuclear Fusion, 62 (7), Art.-Nr.: 074003. doi:10.1088/1741-4326/ac5d61

Shcherbinin, V. I.; Avramidis, K. A.; Thumm, M.; Jelonnek, J. (2022). Design of a High-Q Diamond-Loaded Cavity for a Third-Harmonic Subterahertz Gyrotron Driven by a Low-Power Electron Beam. IEEE Transactions on Electron Devices, 69 (6), 3386–3392. doi:10.1109/TED.2022.3166125

W7-X Team; Killer, C.; Drews, P.; Grulke, O.; Knieps, A.; Nicolai, D.; Satheeswaran, G.; Gantenbein, G.; Huber, M.; Illy, S.; Jelonnek, J.; Kobarg, T.; Lang, R.; Leonhardt, W.; Mellein, D.; Papenfuß, D.; Thumm, M.; Wadle, S.; Weggen, J. (2022). Reciprocating probe measurements in the test divertor operation phase of Wendelstein 7-X. Journal of Instrumentation, 17 (03), Art.-Nr.: P03018. doi:10.1088/1748-0221/17/03/P03018

Adya, S.; Yuvaraj, S.; Rawat, M.; Kartikeyan, M. V.; Thumm, M. K. (2022). Investigations on RF Behavior of a V-Band Second Harmonic Gyrotron for 100/200 kW Operation. IEEE Transactions on Plasma Science, 50 (2), 222–228. doi:10.1109/TPS.2022.3140350

Fable, E.; Janky, F.; Treutterer, W.; Englberger, M.; Schramm, R.; Muraca, M.; Angioni, C.; Kudlacek, O.; Poli, E.; Reich, M.; Siccinio, M.; Tardini, G.; Weiland, M.; Wu, C.; Zohm, H.; ASDEX Upgrade Team. (2022). The

modeling of a tokamak plasma discharge, from first principles to a flight simulator. Plasma Physics and Controlled Fusion, 64 (4), Art.-Nr.: 044002. doi:10.1088/1361-6587/ac466b

Ell, B.; Pagonakis, I. G.; Wu, C.; Gantenbein, G.; Illy, S.; Rzesnicki, T.; Stanculovic, S.; Thumm, M.; Weggen, J.; Jelonnek, J. (2022). Mechanical Design of the Short Pulse E×B Drift Two-Stage Depressed Collector Prototype for High Power Gyrotron. 2021 22nd International Vacuum Electronics Conference (IVEC), 1–2, Institute of Electrical and Electronics Engineers (IEEE). doi:10.1109/IVEC51707.2021.9722425

Ruess, T.; Avramidis, K. A.; Gantenbein, G.; Ioannidis, Z.; Illy, S.; Jin, J.; Pagonakis, I. G.; Rzesnicki, T.; Thumm, M.; Weggen, J.; Jelonnek, J. (2022). Performance Expectation and Preparation of the First Experimental Campaign of the KIT 2 MW 170/204 GHz Coaxial-Cavity Gyrotron. 2021 22nd International Vacuum Electronics Conference (IVEC), 1–2, Institute of Electrical and Electronics Engineers (IEEE). doi:10.1109/IVEC51707.2021.9722448

Rzesnicki, T.; Ioannidis, Z. C.; Avramidis, K. A.; Chelis, I.; Gantenbein, G.; Hogge, J.; Illy, S.; Jelonnek, J.; Jin, J.; Leggieri, A.; Legrand, F.; Pagonakis, I. G.; Sanchez, F.; Thumm, M. (2022). Experimental Testing of the European TH1509U 170-GHz 1-MW CW Industrial Gyrotron – Long Pulse Operation. IEEE electron device letters, 43 (4), 623–626. doi:10.1109/LED.2022.3152184

Mondal, D.; Yuvaraj, S.; Rawat, M.; Thumm, M. K. A.; Kartikeyan, M. V. (2022). Realistic Design Studies on a 300-GHz, 1-MW, DEMO-Class Conventional-Cavity Gyrotron. IEEE Transactions on Electron Devices, 69 (3), 1442–1450. doi:10.1109/TED.2022.3146101

W7-X Team; Brunner, K. J.; Knauer, J.; Meineke, J.; Cu Castillo, H. I.; Hirsch, M.; Kursinski, B.; Stern, M.; Wolf, R. C.; Gantenbein, G.; Huber, M.; Illy, S.; Jelonnek, J.; Kobarg, T.; Lang, R.; Leonhardt, W.; Mellein, D.; Papenfuß, D.; Thumm, M.; Wadle, S.; Weggen, J. (2022). Sources for constellation errors in modulated dispersion interferometers. Review of scientific instruments, 93 (2), Art.-Nr.: 023506. doi:10.1063/5.0070041

W7-X Team; Zhao, D.; Brezinsek, S.; Yi, R.; Oelmann, J.; Cai, L.; Wu, F.; Sergienko, G.; Rasinski, M.; Mayer, M.; Dhard, C. P.; Naujoks, D.; Gantenbein, G.; Huber, M.; Illy, S.; Jelonnek, J.; Kobarg, T.; Lang, R.; Leonhardt, W.; Mellein, D.; Papenfuß, D.; Thumm, M.; Wadle, S.; Weggen, J. (2022). Investigation of boron distribution and material migration on the W7-X divertor by picosecond LIBS. Physica scripta, 97 (2), Article no: 024005. doi:10.1088/1402-4896/ac4a93

W7-X Team; Szűcs, M.; Szepesi, T.; Biedermann, C.; Cseh, G.; Jakubowski, M.; Kocsis, G.; König, R.; Krause, M.; Perseo, V.; Puig Sitjes, A.; Gantenbein, G.; Huber, M.; Illy, S.; Jelonnek, J.; Kobarg, T.; Lang, R.; Leonhardt, W.; Mellein, D.; Papenfuß, D.; Thumm, M.; Wadle, S.; Weggen, J. (2022). Detecting Plasma Detachment in the Wendelstein 7-X Stellarator Using Machine Learning. Applied Sciences, 12 (1), Art.Nr.: 269. doi:10.3390/app12010269

W7-X Team; Knieps, A.; Suzuki, Y.; Geiger, J.; Dinklage, A.; Zhou, S.; Rahbarnia, K.; Schilling, J.; Neuner, U.; Thomsen, H.; Jakubowski, M.; Koenig, R.; Endler, M.; Gao, Y.; Sitjes, A. P.; Niemann, H.; Beurskens, M.; Bozhenkov, S.; Liang, Y.; Gantenbein, G.; Huber, M.; Illy, S.; Jelonnek, J.; Kobarg, T.; Lang, R.; Leonhardt, W.; Mellein, D.; Papenfuß, D.; Thumm, M.; Wadle, S.; Weggen, J. (2022). Plasma beta effects on the edge magnetic field structure and divertor heat loads in Wendelstein 7-X high-performance scenarios. Nuclear fusion, 62 (2), Art.Nr.: 026011. doi:10.1088/1741-4326/ac3a18

W7-X Team; Beurskens, M. N. A.; Angioni, C.; Bozhenkov, S. A.; Ford, O.; Kiefer, C.; Xanthopoulos, P.; Turkin, Y.; Alcusón, J. A.; Baehner, J. P.; Beidler, C.; Birkenmeier, G.; Fable, E.; Fuchert, G.; Geiger, B.; Grulke, O.; Hirsch, M.; Jakubowski, M.; Laqua, H. P.; Langenberg, A.; Lazerson, S.; Pablant, N.; Reisner, M.; Schneider, P.; Scott, E. R.; Stange, T.; Stechow, A. von; Stober, J.; Stroth, U.; Wegner, T.; Weir, G.; Zhang, D.; Zocco, A.; Wolf, R. C.; Zohm, H.; Gantenbein, G.; Huber, M.; Illy, S.; Jelonnek, J.; Kobarg, T.; Lang, R.; Leonhardt, W.; Mellein, D.; Papenfuß, D.; Thumm, M.; Wadle, S.; Weggen, J. (2022). Confinement in electron heated

plasmas in Wendelstein 7-X and ASDEX Upgrade; the necessity to control turbulent transport. Nuclear fusion, 62 (1), ArtNr.: 016015. doi:10.1088/1741-4326/ac36f1

W7-X Team; Brezlnsek, S.; Dhard, C. P.; Jakubowski, M.; König, R.; Masuzaki, S.; Mayer, M.; Naujoks, D.; Romazanov, J.; Schmid, K.; Schmitz, O.; Zhao, D.; Balden, M.; Brakel, R.; Butterschoen, B.; Dittmar, T.; Drews, P.; Effenberg, F.; Elgeti, S.; Ford, O.; Fortuna-Zalesna, E.; Fuchert, G.; Gao, Y.; Goriaev, A.; Hakola, A.; Kremeyer, T.; Krychowiak, M.; Liang, Y.; Linsmeier, C.; Lunsford, R.; Motojima, G.; Neu, R.; Neubauer, O.; Oelmann, J.; Petersson, P.; Rasinski, M.; Rubel, M.; Sereda, S.; Sergienko, G.; Sunn Pedersen, T.; Vuoriheimo, T.; Wang, E.; Wauters, T.; Winters, V.; Zhao, M.; Yi, R.; Gantenbein, G.; Huber, M.; Illy, S.; Jelonnek, J.; Kobarg, T.; Lang, R.; Leonhardt, W.; Mellein, D.; Papenfuß, D.; Thumm, M.; Wadle, S.; Weggen, J. (2022). Plasma–surface interaction in the stellarator W7-X: conclusions drawn from operation with graphite plasma-facing components. Nuclear fusion, 62 (1), Art.Nr.: 016006. doi:10.1088/1741-4326/ac3508

Ruess, T.; Gantenbein, G.; Ioannidis, Z.; Rzesnicki, T.; Wagner, D.; Thumm, M.; Jelonnek, J. (2022). Frequency and mode measurement techniques for megawatt-class gyrotrons. Technisches Messen, 89 (2), 85–96. doi:10.1515/teme-2021-0039

2 Materials and Technologies for the Energy Transition (MTET): - Bioenergy, Concentrated Solar Power and High Temperature Storage -

Contact: Prof. Dr.-Ing. Georg Müller

In the field of bioelectrics, the IHM is doing research in the field of biorefinery concepts for the conversion of microbial biomass, such as microalgae or heterotrophic organisms, into energy carriers and usable materials. One focus is on the development of energy-efficient bioprocesses using pulsed electric fields (electroporation) for cascade processing and thus the most complete possible biomass utilization. As part of a project (ELEGANT) funded by the Agency for Renewable Resources (FNR) research has been carried out on electroporation of yeasts for upcycling agro-industrial residues into bio-lubricants.

2.1 PEF-Processing of Microbial Biomass

Contact: Dr. Wolfgang Frey

2.1.1 ELEGANT: Biobased Lubricants from Oleaginous Yeasts

Compared to lipids from microalgae, oils from oleaginous yeasts exhibit a considerably lower content of (poly)unsaturated fatty acids. This results in a higher stability against oxidation and makes them more suitable as baseoils for bio-lubricants. In addition, oleaginous yeasts can grow heterotrophically on industrial waste streams, e.g. glycerol, molasses or lignocellulose hydroysates up to biomass densities of around 40 gdw/ltr, which minimizes preconcentation efforts in downstream processing.

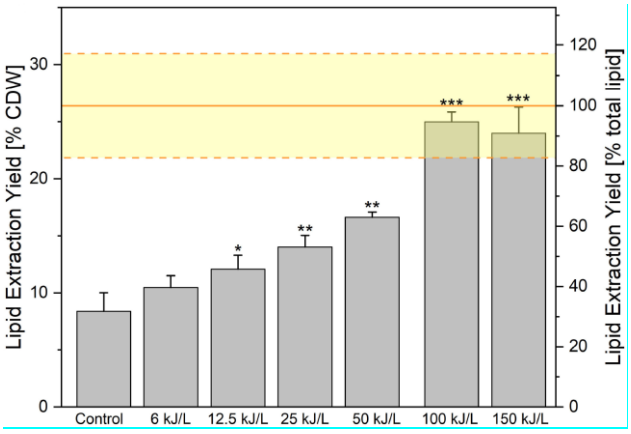

Fig. 2.1.1: Lipid extraction yield over specific treatment energy. PEF treatment with 1µs pulses at 14 kV/cm prior to solvent extration (water/Ethanol/Hexane = 1:18:7.3 vol/vol/vol) results in lipid extraction yields of more than 90% of total lipids when the treatment energy was 100 kJ/ltr and higher, doi: 10.3389/fbioe.2020.575379.

As known from microalgae, oleaginous yeasts also protect their lipid inventory by robust cell walls. Thus, prior to solvent extraction a cell disintegration step is required for achieving high lipid recovery rates.

In collaboration with BLT2, Technical Biology, a first study on the oleaginous yeast *Saitozyma podzolica* could demonstrate that PEF treatment at 100 kJ/ltr allows to recover more than 90 % of the total lipid content from the yeast, while the lipid yield from untreated biomass was only 31 %, Fig. 2.1.1, when applying Ethanol/Hexane blends for solvent extraction in both cases.

These promising results led to a grant application at BMEL/FNR which finally was approved for funding in October 2022. In collaboration with partners from solvent distillation, rheology and lubricant industry, special emphasis will be laid on cascade processing of four different yeast strains for protein and lipid recovery. Extracted proteins and residual biomass will be tested for feed application by University of Hohenheim. Project developments will also focus at optimization of the solvent system in order to minimize costs for solvent recycling, which are a major cost factor in solvent extraction of lipids from wet microbial biomass.

Collaboration: BLT2, Technical Biology

2.1.2 Electrode Corrosion of HV-Electrodes Used for PEF-Treatment of Microalgae Suspensions- Visual Observations and Surface Topology Measurements

Treatment of plants, microbial biomass, etc. with Pulsed Elecctric Fields (PEFs), for food-, feed-pharmaceutical and other applications always implies a direct contact of high voltage (HV) electrodes with the suspension to be processed. Depending on the specified purpose, a high durability and dimensional stability of electrodes are required. According literature, the application of austenitic alloys as electrode material, e.g. A 316 and AISI 316Ti, demonstrates a good resistance against corrosive, especially acidic media and therefore are often used. This type of material, on the other hand, contains high concentrations of nickel, chromium and small amounts of molybdenum. As in most cases, introduction of these components into the processed substrate is only accepted to a minor extent, therefore electrode corrosion effects during PEF-treatment must be considered in more detail.

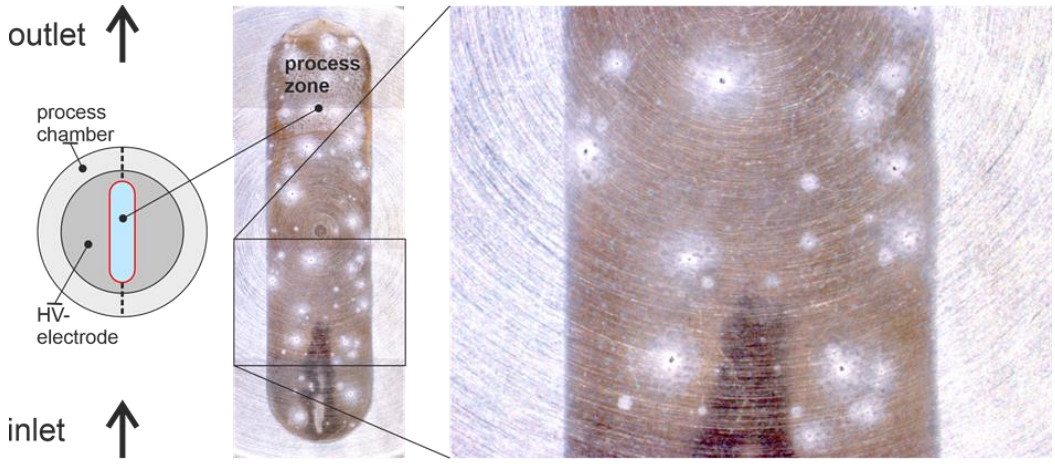

Fig. 2.1.2: Process electrode surface, damaged by corrosion. The images show a uniform surface modification all over the processing zone and isolated corosion spots.

The examination of HV-electrode surfaces used for PEF-processing of concentrated microalgae suspensions and other liquid substrates/electrolytes, show substantial corrosion characteristics, even after a few hours of treatment. Corrosion holes can be identified, almost homogeneously spread across the electrode surface, Fig. 2.1.2, with dimensions ranging from several tens of microns up to hundreds of microns.

After longer PEF-treatment periods of many hours, a large area ablation is visible along the whole PEF-process zone of the HV-electrode which is illustrated by the surface structure measurement-graphic, Fig. 2.1.3. Compared to the electrode surface level outside the PEF-process zone, the lowering of the surface caused by PEF-treatment is clearly visible. Peaks in the surface profile, Fig. 2.1.3, indicate the positions of corrosion-holes at the electrode surface. By weighing of the process electrodes with help of analysis scales, before and after PEF-treatment, removal rates, Δm = 0.25-2.15 mg/h could be observed, depending on electrical parameters, electrode dimensions and processed substrate/electrolyte.

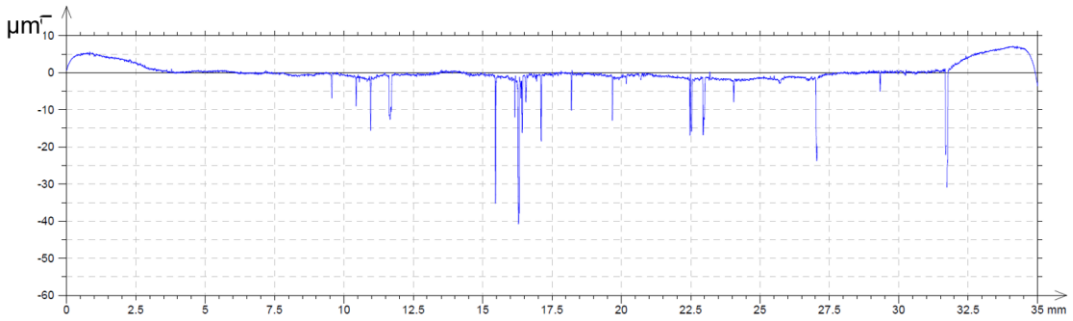

Fig. 2.1.3: Surface profile of the corroded HV-electrode.

Impact of electrodes structural material, processed substrates/electrolytes and processing parameters on electrode corrosion will be investigated in coming evaluations. The corrosion mechanisms, responsible for the identified type of electrode surface damage need to be analyzed. The usage of alternative materials for HV-electrodes will be examined.

2.1.3 Competitive and Mutual Interactions Between Microalgae and Bacteria

This study was supported by the Deutsche Bundesstiftung Umwelt (DBU) as part of an international collaboration with the Centre for Physical Sciences and Technology, Vilnius, Lithuania. Here, we investigated new species-specific co-cultures of microalgae and bacteria that have recently been proposed as a biotechnological strategy to improve the algae growth rates. The use of microalgae-bacteria interactions can be one of the most effective ways to enhance biomass yields and reducing the cost of cultivation. This strategy is particularly advantageous because algae naturally grow in the presence of other microorganisms, where they are prevalent and resilient under extreme conditions.

However, from an industrial point of view, the presence of other microorganisms is often associated with a loss of algae biomass and a decreased purity of co-products. An alternative to avoid contamination with unwanted bacteria is the admixture of microalgal growth promoting bacteria (MGPB) to algal cultures and the promotion of growth through the development of specific interspecies interactions. In this study we found that the type of interaction between microalgae and bacteria is not solely determined by species specificity. Rather, it is a dynamic process of adaptation to the surrounding conditions, where one or the other microorganism dominates (temporally) depending on the growth conditions, in particular the medium composition. For example, when co-cultured on standard nutrient medium (TAP medium), the bacteria had a negative effect on the growth of *C. vulgaris*, whereas co-cultures of algae and bacteria under BG-11 and BG-11+acetic acid resulted in an increase in algae concentration compared to cultures of the same species under the same conditions.

Nevertheless, the growth of heterotrophically cultured *C. vulgaris* (TAP A+B, even if growth was reduced by the presence of bacteria) was significantly higher than under autotrophic and mixotrophic conditions (BG A and BGT A, Fig. 2.1.4 These data suggest that a positive interaction between *C. vulgaris* and bacteria is possible under stress conditions where the organic nutrition source is limited. On the other hand, when medium is full of organic carbon source, negative type of interaction is formed. The ability of both algae and bacteria (independently) to grow successfully in the TAP medium raises the hypothesis of competition for nutrients.

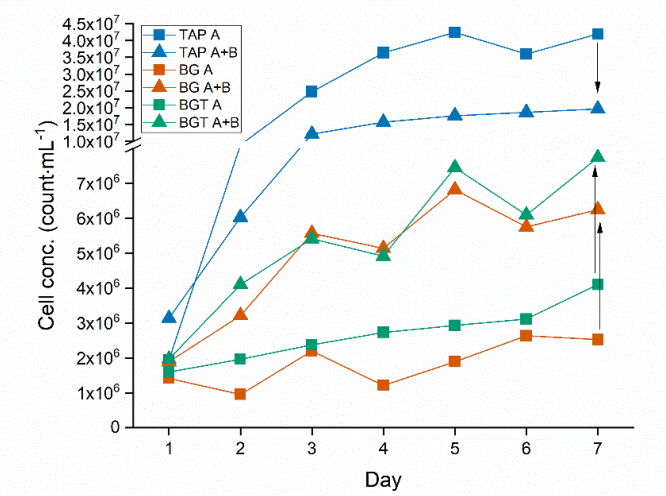

Fig. 2.1.4: Change of cell count during the cultivation process.

This study shows that what is thought to be a symbiotic behavior between bacteria and algae might be just an adaptation of the microorganisms to the surrounding conditions, with one or the other microorganism dominating (temporally) depending on the growth conditions, especially the cultivation medium. We concluded that this bacterial species could be a suitable candidate as an MGPB and could be used for the development of algae technologies. In particular, it can be used to develop environmentally friendly and chemical-free wastewater treatment technologies for open ponds. Nevertheless, further research is needed to understand the interaction between bacteria and algae, especially the competition for nutrients and the mutual interaction.

Collaboration: Centre for Physical Sciences and Technology, Vilnius, Lithuania

2.1.4 Investigations to find the cell death-inducing factor extracted from *C. vulgaris*

The most significant result, obtained in a preceding doctoral thesis, involved the discovery of a cell death inducing factor that can be extracted from *C. vulgaris* in response to PEF treatment or after disrupting the cells by high pressure homogenisation. So far, we know that the cell death inducing factor is produced by the microalga *C. vulgaris* itself, mainly in the stationary phase of 4-7 days after inoculation. Also, it has been shown that it is most likely a protein or a group of proteins. The death factor plays an important role during the algae incubation period for protein extraction after PEF treatment, by triggering programmed cell death in intact cells and subsequent autolytic processes, leading to an enhanced extraction process. We have shown that this already can be achieved at very low specific PEF treatment energies.

This discovery raised two main questions: the first was, how does the protein extract induce cell death in *C. vulgaris*, and, second, whether the death factor is specific for *C. vulgaris*. To answer these questions, a Bachelor's and a Master's thesis have been carried out.

To investigate the specificity of the death factor extracted from *C. vulgaris*, four different species *Chlorella sorokiniana*, *Clamydomonas reinhardtii*, *Microcloropsis salina* and *Nannocloropsis oculata* were selected and treated with *C. vulgaris* extract. In addition, the four species were treated with their own extract with different protein concentrations to assess the distribution of this trait within the different microalgal species. Mortality was quantified by staining live cells with fluorescein diacetate and data were collected by flow cytometry. Apart from *C. sorokinana*, the studied species show a decrease in survival when treated with the protein suspension extracted from *C. vulgaris*. This suggests that other eukaryotic microalgae are susceptible to the death factor extracted from *C. vulgaris*.

On the other hand, only *C. reinhardtii* shows a response to its own protein extract at relatively high protein concentrations, indicating that the death factor is not widely distributed among eukaryotic microalgae. It could be shown that the death factor is already produced at low levels in the cells during the exponential growth phase. In the stationary phase, however, it is present at increased concentrations, and it is probably only then released from extracellular vesicles into the cytosol. This observation suggests that *C. vulgaris* responds to a starvation signal.

In addition, a lethal fraction with a total of 29 proteins could be isolated by activity-guided protein fractionation. Nevertheless, it was not possible to make a clear assignment of the death factor to any of the identified protein candidates. In the next steps, the mechanism of cell death triggered in *C. vulgaris* by its own protein extracts will be investigated using improved activity-guided fractionation. These results will enable the biotechnological application of low energy PEF treatment to other strains of microalgae, providing a sustainable method of cell component recovery.

Collaboration: Botanical Institute, KIT Campus South

2.1.5 Lipid Extraction from Microalgae – Reduction of Overall Downstream Processing Costs

In the past years, our group has demonstrated that pulsed electric field (PEF) was an efficient pre-treatment to enable lipid extraction using ethanol-hexane blends. The lipid extraction process that was developed based on the PEF pre-treatment has many intrinsic advantages: 1) it is a non-thermal process compatible with extraction of thermo-sensitive molecules, 2) it is efficient on wet-biomass and therefore enables to bypass the expensive drying step, 3) it does not generate cell debris which facilitates further down-stream processing, 4) it can easily be upscaled and is well suited for continuous flow processing and 5) the PEF-treatment requires low energy input, typically 0,5 MJ/kg_{DW}.

The main drawback of the existing process was the large amounts of solvent used and consequently the considerable costs for recycling excluding de facto the use of the extracted lipids for low added-value applications such as biofuels. Therefore, efforts were concentrated on reducing volumes of solvents and on a new method to perform extraction using still ethanol and hexane but in a biphasic distribution. In this approach, microalgae are in a water-ethanol mixture and lipids are continuously extracted and transferred to the second organic phase consisting of pure n-Hexane, leaving the water-ethanol phase lipid-free. This approach was successful in extracting the lipids with reduced amount of solvents. The overall down-processing costs were evaluated to reach 62 MJ/kg_{Lipids}, i.e. about six time less than what was required in

the best scenario using the standard ethanol-hexane blend which required 367 MJ/kg_{Lipids}. The clear improvement of the energy balance of the whole downstream process already opens the path to many applications of the extracted lipids in the food or feed industry or for chemical use. Nevertheless, the energy consumption remained too high to consider an energetical usage of the lipids.

Since Ethanol forms an unfavourable azeotrope with water, its recycling is extremely energy demanding and it was responsible for more than half of the energy consumption in the best previous downstream scenario. Therefore, further strategies were investigated with the objective to eliminate ethanol, focusing on the use of non-polar solvents only, which are easier to separate from the remaining water and can be recycled at low cost. From all tested solvent, only two, i.e. MTBE and Ethyl-Acetate, performed relatively well when applied directly on wet pellet with lipid extraction yields above 20 % of cell dry weight (20 $\%_{CDW}$), data not shown.

In order to increase the efficiency of all non-polar solvents or solvents of low polarity, a new approach has been proposed, consisting in extraction in the presence of solvent and an excess of water, 2.1.5. This approach, contrary to the current dogma, that water is unfavourable for solvent extraction, has proven to be very promising when applied on PEF-treated *A. protothecoides,* as can be seen in Fig. 2.1.5. Indeed, in the case that water is added in excess, all tested solvents enable to extract more than 18 $\%_{CDW}$. Hexane and Heptane in particular, which are non-miscible solvents and therefore very easy to recycle, perform well with extraction yields above 25 $\%_{CDW}$ in the presence of an excess of water while they are totally inefficient when applied alone on the wet pellet (yield < 5 $\%_{CDW}$, data not shown). More polar solvents such as 2-Butanol also appear much more efficient in the presence of an excess of water with yield of 33 $\%_{CDW}$ versus < 5 $\%_{CDW}$ when applied directly on wet pellet.

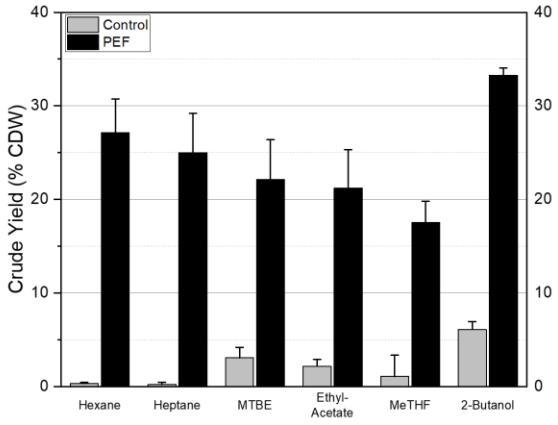

Fig. 2.1.5: Extraction of lipids with non-polar solvents or solvents of low polarity. Solvents were applied together with an excess of water (water:solvent, 2:1, v:v). The experiments were performed on fresh A. Protothecoides with 30 g of dry biomass per litter of solvent. Solvent extraction was either applied directly after harvesting (Control) or after pulsed electric field (PEF) treatment. Results are the average + std of three independent experiments. Note that the y-axis is labelled crude yield but that analyses have demonstrated a lipid purity in the extract above 98%. Total lipid content was evaluated to be 40.4±4.0 $\%_{CDW}$. Control values denote extraction yields for the same processing chain, but without PEF treatment.

It was also demonstrated that such an extraction strategy remains efficient at high biomass to solvent ratio, a prerequisite for the process to be viable at industrial scale. The results for Hexane respectively 2-Butanol applied with an excess of water are shown on Fig. 2.1.6 increasing the biomass:solvent ratio from 30 g/L to 300 g/L resulted in a slight decrease of the yields: from 32 $\%_{CDW}$ to 24 $\%_{CDW}$ in the case of Hexane and from 35 $\%_{CDW}$ to 29 $\%_{CDW}$ in the case of 2-Butanol. However, the high yields still obtained at 300 g/L solvent allow to consider an upscaling and an industrial implementation. Interestingly, those findings are also

contradicting a consensus of the literature which states that when extraction is performed with a solvent which is non-miscible with water, i.e. a non-polar solvent, such as Hexane or solvent of low polarity, a preliminary cell disruption step is required mandatorily to disrupt the cell wall and therefore give solvent access to the lipids. Avoiding this disruption step is the guarantee to keep the overall structure of the microalgae intact. This has the effect of avoiding debris and limiting emulsion formation, two aspects that greatly facilitate the rest of the downstream processing.

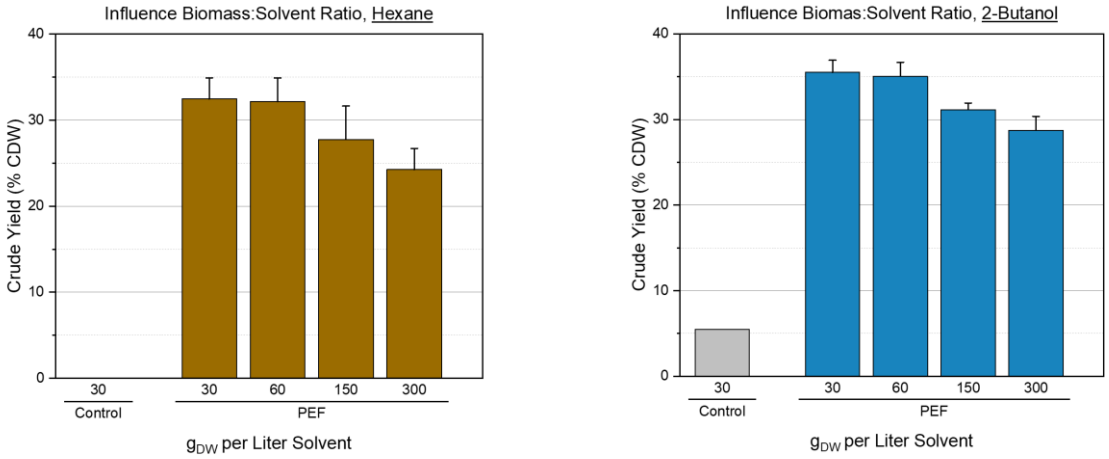

Fig. 2.1.6: Impact of the Biomass: Solvent ratio on the extraction yield using either n-Hexane (left) or 2-Butanol (right) as an organic solvent and an excess of water. Experiments were performed on fresh *A. protothecoides*. Results are the average + std of 2 independent experiments.

The estimated energy required for the whole downstream process ranges from 7.34 MJ/kg_{lipid} to 16.68 MJ/kg_{lipid} for *A. protothecoides* which requires PEF-treatment but simple process improvements, such as the reduction of the PEF energy, can reasonably predict a further strong reduction of the required energy. For some other microalgae, which do not require any pre-treatment, the energy required ranges from 2.05 to 6.47 MJ/$kg_{biodiesel}$. The low energy requirements which are in some cases less than 10 % of the energy content of the lipids, opens the path to energetical applications of microalgae lipids.

2.1.6 Influence of biomass concentration on the pH of microalgae suspension and the impact of incubation pH on the lipid extraction assisted by PEF from *A. prothotecoides*

The interest on oleaginous microalgae has increased in the last years as a promising source of lipids for biodiesel usage, in which IHM has developed a great expertise in the application of Pulsed Electric Fields for their facilitated extraction. However, there is still an overall optimization of the assisted lipid extraction by PEF from microalgae required in order to be a competitive strategy. In this context, an evaluation of the concentration of the microalgae biomass along with the influence of the medium pH on the final lipid yield was carried out.

The microalgae *Auxenochlorella prothotecoides* grown under mixotrophic conditions was used in this study. The lipid yield and electroporation level of PEF-treated *A. protothecoides* were determined at a medium pH of 3.0 and 5.0 under variation of the pre- or post-PEF incubation time and for split-dose treatments.

Low energetic PEF treatments with 40 kV/ cm and 1 µs pulses at 9.6 kJ/L and 19.2 kJ/L were performed either in batch mode or in continuous flow.

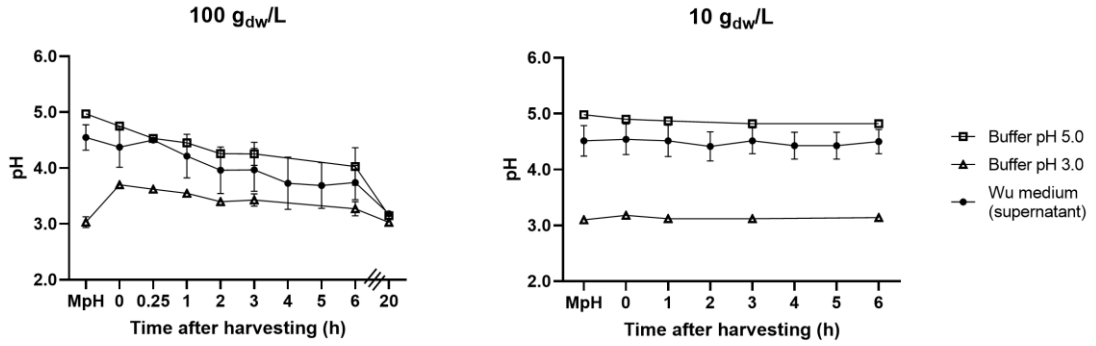

Fig. 2.1.7: pH evolution along time after resuspend (A) concentrated (100 gdw/L) and (B) non-concentrated (10 gdw/L) microalga biomass in its own medium, McIlvaine buffers at pH 3.0 and 5.0. MpH: Original pH of supernatant and buffers media before resuspending microalgae cells.

The concentration (from 10 to 100 g_{dw}/L) of the microalgae biomass resulted in a progressive variation of the pH going up to 2 points of difference during 6 hours after harvesting, even when the resuspensions were made in buffer media, Fig. 2.1.7 left.

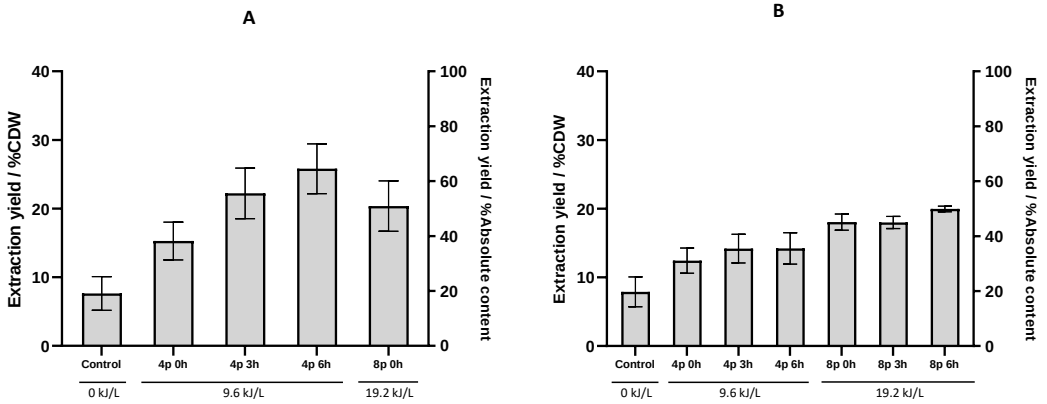

Fig. 2.1.8: Influence of incubation after PEF on the lipid extraction yield obtained by PEF treatments (40 kV/cm) of 4 pulses (9.6 kJ/kg) and 8 pulses (19.2 kJ/kg) at pH 3.0 (A) and 5.0 (B).

Conversely, for unconcentrated conditions, the pH of microalgae suspension was maintained, Fig. 2.1.8, right. Further experiments performed under non-concentrated conditions (10 g_{dw}/L) at different pH showed that pre-PEF-incubation did not influence the electroporation or the lipid extraction. However, post-PEF incubation significantly increased the share of electroporated cells (> 60 %) in medium pH 3.0, while no change was observed at pH 5.0, Fig. 2.1.8.

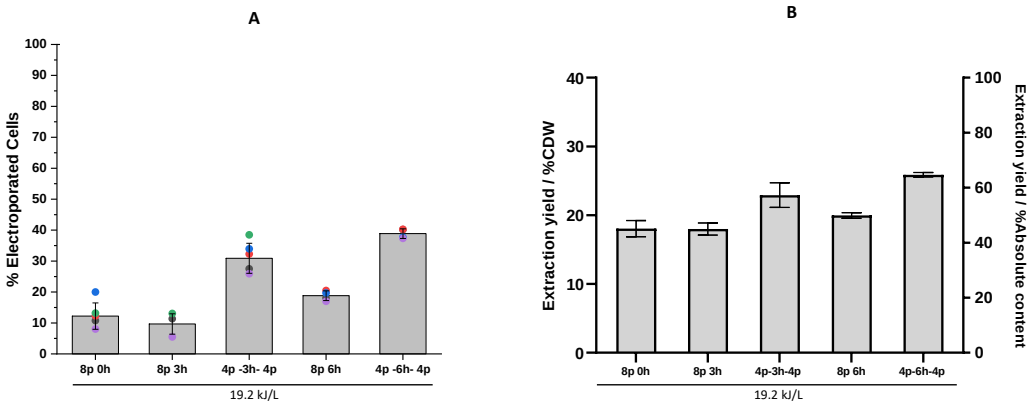

Fig. 2.1.9: Influence of split-dose PEF treatment at pH 5.0 on the percentage of electroporation levels (A) and lipid extraction yields (B) obtained by PEF treatments (40 kV/cm) of 8 pulses (19.2 kJ/L) applied as a singles dose of 8 pulses or split into two trains as 4+4 pulses with 3 or 6 hours between them.

Split-dose PEF treatments at pH 5.0 caused significantly higher electroporation levels and lipid extraction yields than equivalent single-dose treatments, Fig. 2.1.9. Results showed that medium pH is critical in the final electroporation and lipid extraction yields of *A. protothecoides* and therefore should be considered in further studies.

Collaboration: University of Zaragoza, Faculty of Veterenary

2.2 Components and Electroporation Processes

Contact: PD Dr. Martin Sack

2.2.1 Semiconductor-based Marx-type Pulse Generator for PEF-treatment of Potatoes

For the PEF-treatment of potatoes in industrial scale a 32-stage Marx-type pulse generator equipped with IGBT switches has been set up. The generator features a stage voltage of up to 800 V and is designed for a peak pulse current of up to 500 A into an RLC pulse circuit with a pulse length of approximately 10 µs. Fig. 2.2.1 shows a photo of the generator. As the generator will be operated in groud-symmetric configuration, it has been split into two stacks, each consisting of 16 stage modules and grounded at its center terminal. In the course of the continuing tests, the generator has been operated connected to an artificial load at a stage voltage of 800 V, a pulse repetiton rate of 100 Hz, and a peak current of 600 A, which is slightly above the rated current of the modules. Fig. 2.2.2 shows the output voltages measured versus ground at the terminals of both stacks and the current. The inductance of the pulse circuit and the total discharge of the pulse capacitors during the pulse both enable energy-efficient soft switching during turn-on and turn-off of the switchesFig. 2.2.3 shows voltages and currents when closing the pulse switches. The output voltage rises within approximately 100 ns.

The generator features a resonant charging circuit, which is fed from a voltage source. This design allows for charging the stage capacitors to approximately twice the voltage delivered by the voltage source. As the charging circuit comprises passive components only, i.e. chokes, capacitors, and diodes, the IGBT switches are the only switches in the pulse circuit, which are actively controlled. The charging voltage can be fine-tuned by a modulation of the on-time of the IGBT switches for pulse generation. Fig. 2.2.4 shows a variation of the charging current and charging voltage by approximately 4 % when doubling the on-time of the switches from 50 µs to 100 µs with the generator powered from a source voltage of 55 V.

Fig. 2.2.1:-stage Marx generator connected to an artificial load.

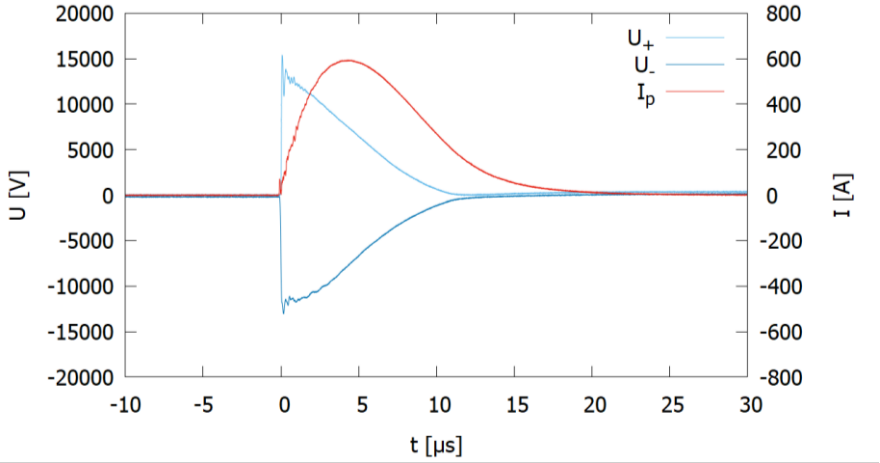

Fig. 2.2.2: Ground-symmetric operation of 32 stages at Vstage = 780 V and frep = 100 Hz: Voltages and current at the genertor's positive and negative output terminal.

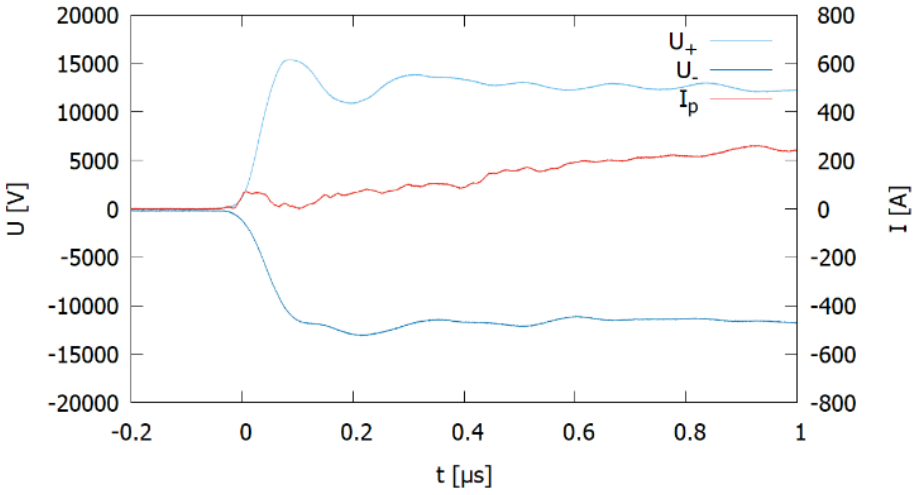

Fig. 2.2.3: Ground-symmetric operation of 32 stages at Vstage = 780 V and frep = 100 Hz: Closing of the pulse switches under soft-switching conditions.

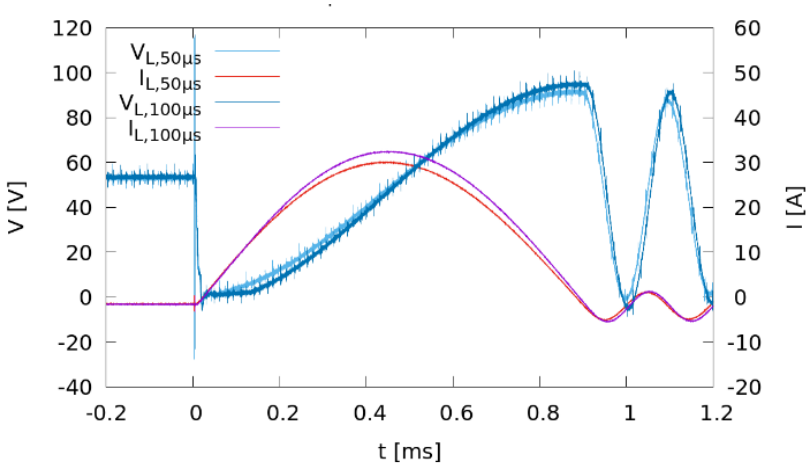

Fig. 2.2.4: Modulation of switches' on-time: ton = 50 µs vs. ton = 100 µs.

2.2.2 Generator Development for Driving a Stripline Kicker

In the frame of a cooperation with DESY, Hamburg, a pulse generator for driving a stripline kicker is currently being developed. For the purpose of design evaluation and component testing 4-stage pulse generators featuring gate-boosted operation of SiC MOSFETs and separate capacitor chargers at each stage. Thereby, the power is transferred to the stages from an AC current source via transformers. Fig. 2.2.7 shows a simplified equivalent circuit and Fig. 2.2.6 a photo of the test setup.

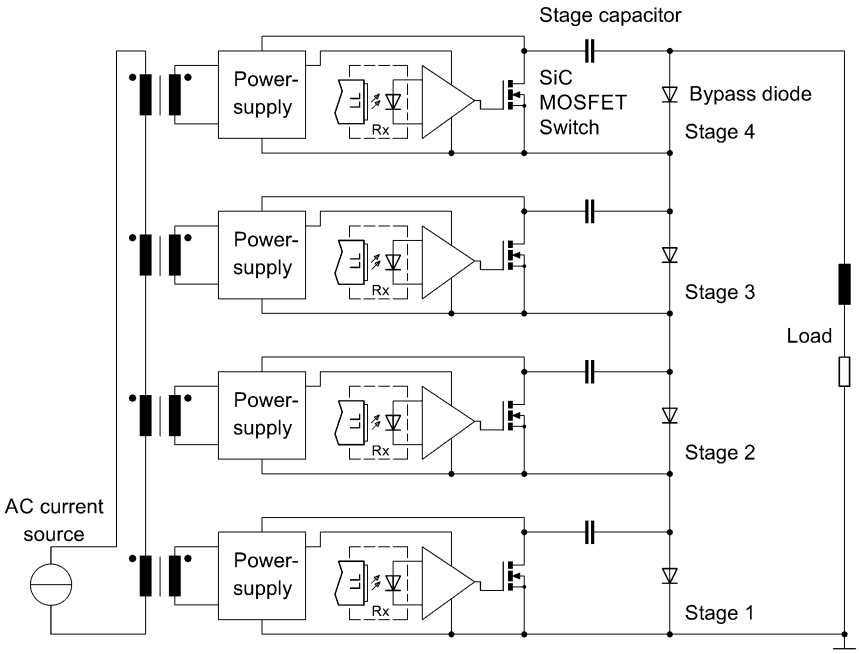

Fig. 2.2.5: Simplified equivalent circuit of the pulse generator.

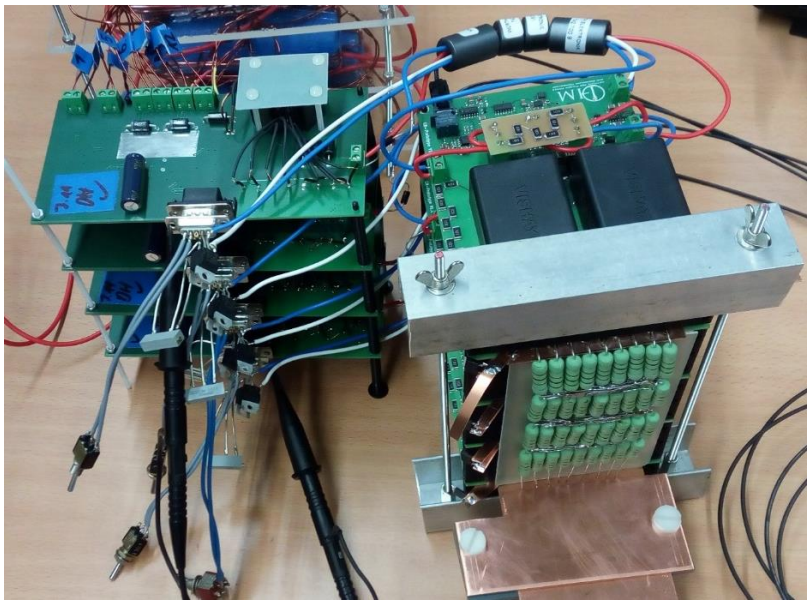

Fig. 2.2.6: Photo of the pulse generator

The generator has been operated so far up to a voltage of 600 V per stage connected to a resistive load of 44 Ohm. Fig. 2.2.7 shows the output voltage for a pulse length of 75 µs. Due to the discharge of the stage capacitors the output voltage exhibits some droop. Fig. 2.2.8 shows the leading edge of the pulse. The output voltage rises to approximately -2.4 kV within a rise time of 3.9 ns (measured between 10% and 90% of the peak voltage). The trigger signal occurs approximately 25 ns before begin of pulse generation.

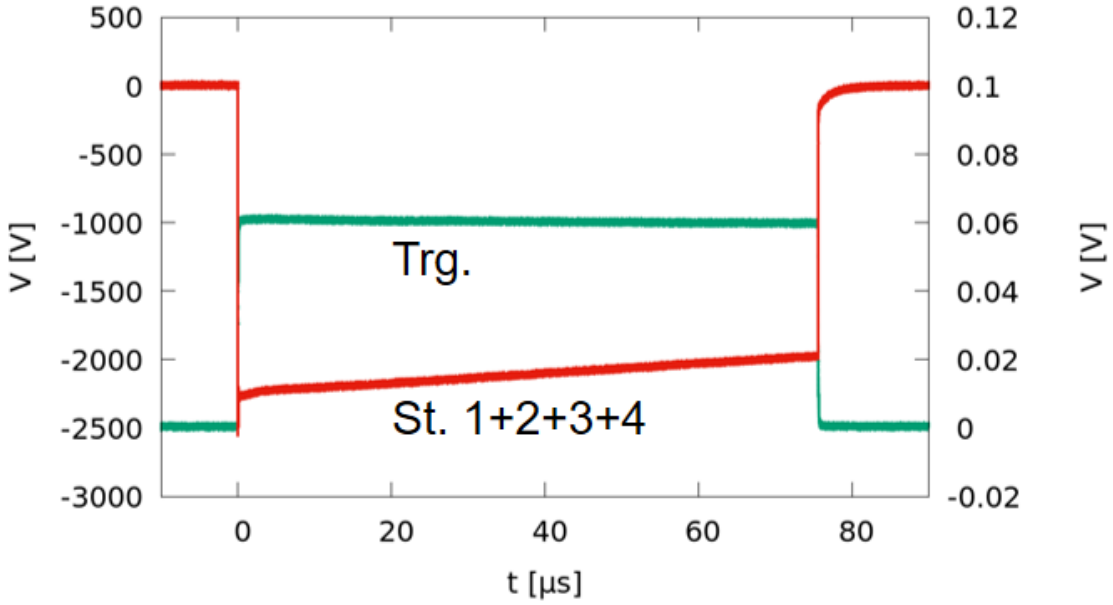

Fig. 2.2.7:- Output voltage of the 4-stage generator measured across a resistive load of 44 Ohm.

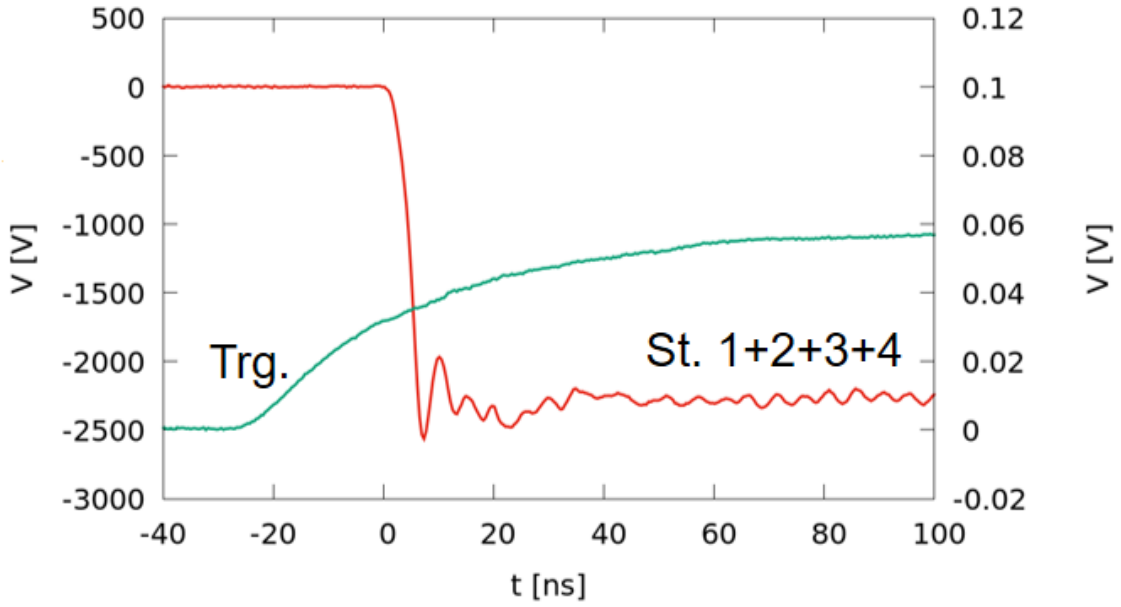

Fig. 2.2.8: Leading edge of the generator's output voltage measured across a resistive load of 44 Ohm.

2.3 Concentrating Solar Power (CSP) and High Temperature Thermal Storage / Liquid Metal – Material Compatibility

Contact: Dr. Alfons Weisenburger, Prof. Dr.-Ing. Georg Müller

Liquid metals as advanced heat-transfer (HTM) and storage media for CSP and other high temperature technologies are a promising research area that will result in performance and efficiency increase and reduced costs. Within LIMCKA (Liquid Metal Competence Center KArlsruhe) several institutes and laboratories of the KIT combine their long-standing experience and specific expertise in material research, system engineering, safety and thermal-hydraulics to tackle all relevant aspects of liquid metals as HTM. The IHM focuses on compatibility research by surface optimization of existing materials using GESA and development of new materials that are able to mitigate corrosion in contact with liquid metals and salts. Liquid metal batteries are a further research area where the expertise of the IHM and DLR is combined with the expertise of a Chinese university (HUST) to explore Sb-Bi(Sn)/Na based low cost liquid metal battery concepts in the frame of a German-Chinese DFG project. The technical feasibility and scaling of CO_2-free methane pyrolysis in liquid high-temperature Sn (> 1000 °C) is investigated as part of the DECAGAS project together with ITES and WINTERSHALL-DEA. Components (valves, pumps) for a high temperature storage based on liquid Pb are under investigation in the BMWi funded project LIMELISA together with the ITES, DLR and coordinated by the company KSB. In this project IHM investigates the compatibility of materials in Pb up to 700 °C and propose potential candidates for the manufacturing of pumps and valves to be used in such conditions.

Some of the tasks are embedded in European projects, the EERA-CSP and cooperations like with DLR and HUST via the DFG or with KSB and DLR via the BMWi or in a direct industrial cooperation.

The most relevant results obtained in the reporting period are presented briefly:

2.3.1 CSP – experimental set-up transient heat loads

Contact: Dr. Alfons Weisenburger

An experimental setup to investigate material compatibility during transient heat loads in a CSP sodium receiver was built. The high-temperature sodium loop SOLTEC-2 was combined with an inductive heater to generate transient heat loads in a U-shaped test tube. The loop was successfully transferred to the new location at the IHM laboratory and taken again in operations with a heated dummy test section first. This recommissioning after changing the installation location clearly demonstrates the robustness of the loop design.

2.3.2 Material development

Contact: Dr. Annette Heinzel, Anisa Purwitasari, Dr. Ceyhun Oskay, Dr. Alfons Weisenburger

Corrosion tests in liquid Na and Na-vapor at 450 °C of several metallic and ceramic materials clearly demonstrated the overall good compatibility of many kinds of materials with liquid and vaporized sodium in the medium temperature range. Tests at 700 °C and thermal cycling tests in flowing sodium are targeted with the new SOLTEC facility available at the IHM.

In cooperation with the DLR in Stuttgart Fe-based alloys (In800H and stainless steel 310) were exposed in Mg purified $MgCl_2$-KCl-NaCl molten salts at 700 °C for 2000h. Adding 2.8 wt% Mg reduced the corrosion rate of the steel 310 to < 7.6 µm/year and that of alloy In800H to 4.9 µm/year. The concentration of the corrosive impurity, MgOHCl is reduced by the addition of 2.8 wt% Mg to 200 ppm, which seems to be an acceptable impurity level for the use of Fe-based alloy in molten Mg-Chloride salts.

Based on exposure tests of different ceramic materials in liquid Sn at temperatures of 800 °C, 950 °C, 1000 °C, 1100 °C for up to 10.000 h the most suitable material was selected together with the ITES and the industrial partner Wintershall-DEA and proposed for an upscaling step of the direct methane pyrolysis in liquid Sn. A SiN infiltrated SiC as potential tube material and a Mg-Alumina-spinel brick as lining material were selected for the different design options.

In the framework of the LIMELISA project funded by BMWi, the shortlisted material candidates for pump and valve were tested in stagnant liquid lead with $2x10^{-7}$ wt% oxygen at 600 °C and 700 °C for 5000 h. After 2000 h exposure, severe dissolution attacks were observed in aluminized materials 316Ti and Ni-based alloy 718 (via pack cementation), indicating that aluminide coating itself is not sufficient to inhibit Pb infiltration. A pre-oxidation treatment which aims to form a thin alumina scale on aluminized materials before exposing them to liquid lead was found to be effective against dissolution attacks and allows material application up to 700 °C. Furthermore, the surface under the alumina scale still has sufficient Al. Aluminized P91 showed similarly excellent behavior at temperatures up to 700 °C.

Another promising structural material that has been included recently into the study due to its excellent mechanical creep resistance is Alloy 800H, which suffered from dissolution attacks and selective dissolution of Ni. Aluminization followed by pre-oxidation is proposed for this material as well and will be explored.

The alumina-forming FeCrAl Kanthal APM exhibited excellent resistance at 600 °C while internal oxidation was observed after exposure at 700 °C. This indicates that between 2000 h and 5000 h the alumina scale has failed and the oxygen inward diffusion rate was higher than the outward diffusion rate of Al, since no internal oxidation after 2000 h exposure was visible. Adequate corrosion resistance at 700 °C was also demonstrated for the Co-based alloy Stellite 6 due to the formation of a continuous and dense chromia scale and of technical ceramics with Ni-Cr and Co binder.

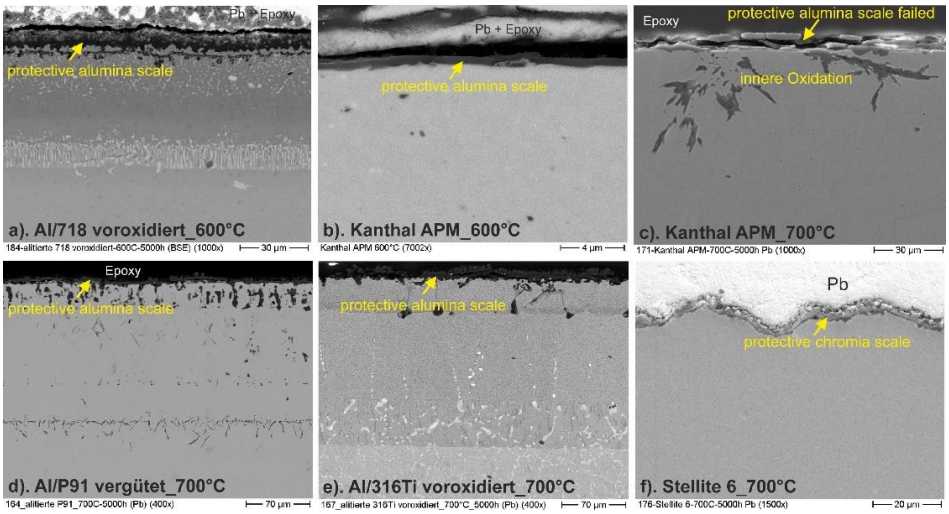

Fig. 2.3.1:-: Cross sectional SEM images after 5000 h exposure. a) aluminized and pre-oxidized Inconel 718 at 600°C, b) Kanthal APM at 600°C, c) Kanthal APM at 700°C, d) quenched and tempered aluminized P91 at 700°C, e) aluminized and pre-oxidized 316Ti at 700°C.

2.3.3 Liquid metal battery

Contact: Dr. Renate Fetzer, Tianru Zhang, Dr. Annette Heinzel, Dr. Alfons Weisenburger

Liquid metal batteries (LMBs) are characterized by an easy scalability and long life, which makes them particularly suitable for large-scale energy storage to stabilise the power grids for the expansion of volatile renewable energies. At our institute, sodium (Na) was investigated as potential negative electrode material, which brings economic and environmental advantages over other LMBs using, for instance, lithium. The active components of a Na-LMB comprise liquid Na as negative electrode, a molten salt as electrolyte, and a heavy liquid metal as positive electrode. The higher working temperature of LMBs compared with conventional batteries leads to an increased corrosion of the solid cell components. Here, the corrosivity of the heavy liquid metal alloy towards structural materials (the cell body) is of most concern.

To mitigate corrosion issues and self-discharge of Na-LMB cells, a low operating temperature is targeted. A promising salt is the chloride system LiCl-NaCl-KCl, which combines a high Na^+ conductivity with a low melting temperature. Heavy metals that are potentially suitable for the positive electrode are the alloy systems Sb-Sn and Sb-Bi due to their electrochemical activity against Na and low melting temperature. In respective corrosion experiments performed for 750 h at 450 °C, the operating temperature of the envisaged Na-LMB cells, the corrosivity of Sb-Sn and Sb-Bi alloys in different compositions towards various candidate structural materials (f/m steel T91, austenitic steels SS 304 and SS 316L, Kovar 4J33, Cr, Mo, and MAX phase coatings) was investigated. Sb-Bi alloys with low amount of Sb were found to be least aggressive towards structural materials and were thus selected for further testing in Na-LMB cells. Excellent corrosion resistance was found for Mo and MAX-phases, while the corrosion rate of steels is acceptable only for short-term application.

In addition to material compatibility research, an LMB manufacturing and testing facility was set up. Cell design and assembly procedures were researched and improved until a fully operational cell was obtained. The final prototype Na-LMB cells with 5 Ah nominal capacity were made from austenitic steel SS 316Ti (cell body), $SbBi_9$ alloy as positive electrode, molten salt LiCl-NaCl-KCl (61:3:36 at%) as electrolyte, and 4.5-5.0 g of Na hosted by a Ni foam Fig. 2.3.2). The Na-LMB test cells achieved excellent performance. With an active material utilization of around 80 %, a Coulombic efficiency > 98 % was achieved, thanks to a low self-discharge around 10 mA (0.35 mA/cm²). The energy efficiency of 70 – 80 % may be further increased by lowering the distance between the electrodes and thus the ohmic overpotential. More than 700 charge/discharge cycles were stably run. However, the capacity continuously decreased during cycling, probably due to corrosion issues of the SS 316L cell body, which limits the long-term application of the LMB cell. Here, a cell body made of Mo is expected to mitigate corrosion and prolong the lifetime of Na-LMB cells.

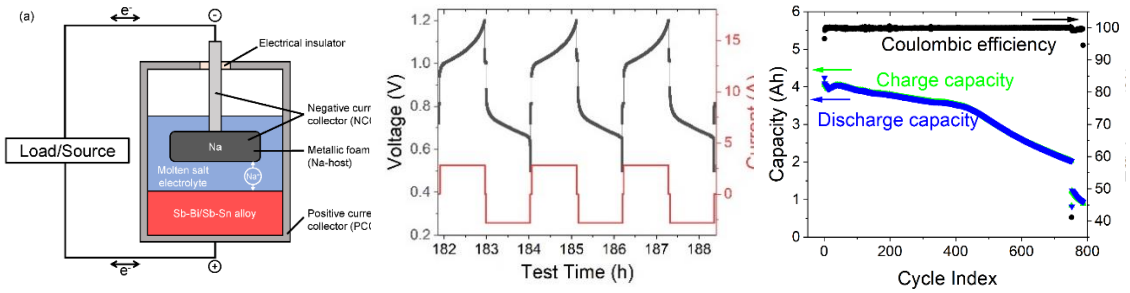

Fig. 2.3.2:- Na-LMB cell with 5 Ah nominal capacity. Schematic of cell (left), typical charge-discharge cycles (middle), cell performance versus cycle index (right).

Journal Publications

Ruf, J.; Barnes, M. J.; Kramer, T.; Sack, M. (2022). Improvements of a Branch Module for an Inductive Voltage Adder Based on Measurements and Circuit Simulations. 2022 IEEE International Power Modulator and High Voltage Conference (IPMHVC), 76–79, Institute of Electrical and Electronics Engineers (IEEE). doi:10.1109/IPMHVC51093.2022.10099414

Sack, M.; Herzog, D.; Ruf, J.; Mueller, G. (2022). Resonant Charging Circuit for a Semiconductor-Based Marx Generator for an Electroporation Device. IEEE International Power Modulator and High Voltage Conference (IPMHVC), Knoxville, TN, June 19-236, 2022, 108–111, Institute of Electrical and Electronics Engineers (IEEE). doi:10.1109/IPMHVC51093.2022.10099422

Sack, M.; Ruf, J.; Herzog, D.; Müller, G. (2022). Modelling of a Resonant Charging Circuit for a Solid-State Marx Generator. Applied Sciences, 12 (23), Art.-Nr.: 12481. doi:10.3390/app122312481

Stephan, F.; Gross, M.; Grebinyk, A.; Aboulbanine, Z.; Amirkhanyan, Z.; Budach, V.; Ehrhardt, V. H.; Faus-Golfe, A.; Frohme, M.; Germond, J.-F.; Good, J. D.; Grüner, F.; Kaul, D.; Krasilnikov, M.; Leavitt, R.; Leemans, W.; Li, X.; Loisch, G.; Müller, F.; Müller, G.; Obier, F.; Oppelt, A.; Philipp, S.; Qian, H.; Reindl, J.; Riemer, F.; Sack, M.; Schmitz, M.; Schnautz, T.; Schüller, A.; Staufer, T.; Stegmann, C.; Tsakanova, G.; Vozenin, M.-C.; Weise, H.; Worm, S.; Zips, D. (2022). FLASHlab@PITZ: New R&D platform with unique capabilities for electron FLASH and VHEE radiation therapy and radiation biology under preparation at PITZ. Physica Medica, 104, 174–187. doi: 10.1016/j.ejmp.2022.10.026

Papachristou, I.; Zhang, S.; Gorte, O.; Ochsenreither, K.; Wüstner, R.; Nazarova, N.; Frey, W.; Silve, A. (2022). Direct transesterification of microalgae after Pulsed Electric Field (PEF) treatment. Journal of Chemical Technology & Biotechnology, 98 (3), 642–650. doi:10.1002/jctb.7293

Gong, Q.; Shi, H.; Chai, Y.; Yu, R.; Weisenburger, A.; Wang, D.; Bonk, A.; Bauer, T.; Ding, W. (2022). Molten chloride salt technology for next-generation CSP plants: Compatibility of Fe-based alloys with purified molten MgCl2-KCl-NaCl salt at 700 °C. Applied Energy, 324, Art.-Nr.: 119708. doi:10.1016/j.apenergy.2022.119708

Delso, C.; Silve, A.; Wüstner, R.; Nazarova, N.; Álvarez, I.; Raso, J.; Frey, W. (2022). Post-incubation pH Impacts the Lipid Extraction Assisted by Pulsed Electric Fields from Wet Biomass of Auxenochlorella protothecoides. ACS Sustainable Chemistry & Engineering, 10 (37), 12448–12456. doi:10.1021/acssuschemeng.2c04016

Shi, H.; Wu, T.; Gong, Q.; Ding, W.; Chai, Y.; Weisenburger, A.; Chang, L.; Zhang, Z.; Wang, K.; Richter, J.; Niendorf, T.; Müller, G. (2022). Hot corrosion behavior of additively manufactured stainless steel 316L and Inconel 718 in MgCl2/KCl/NaCl chloride salts at 700 °C. Corrosion Science, 207, Art.-Nr.: 110561. doi:10.1016/j.corsci.2022.110561

Onea, A.; Hering, W.; Ulrich, S.; Rieth, M.; Weisenburger, A.; Reiser, J.; Lenk, S.; Röbert, T.; Vielhaber, S.; Baumgärtner, S.; Ziegler, R.; Stieglitz, R. (2022). Innovative 1000K sodium loop for qualification of new materials for applications in CSP field. SOLARPACES 2020: 26th International Conference on Concentrating Solar Power and Chemical Energy Systems, 020010, AIP Publishing. doi:10.1063/5.0087110

Niedermeier, K.; Mueller-Trefzer, F.; Daubner, M.; Marocco, L.; Weisenburger, A.; Wetzel, T. (2022). Theoretical and experimental studies of dual-media thermal energy storage with liquid metal. 26th

International Conference on Concentrating Solar Power and Chemical Energy Systems (SolarPACES 2020), Article no: 160011, AIP Publishing. doi:10.1063/5.0085881

Zhang, Y.; Soldatov, S.; Papachristou, I.; Nazarova, N.; Link, G.; Frey, W.; Silve, A. (2022). Pulsed microwave pretreatment of fresh microalgae for enhanced lipid extraction. Energy, 248, Art.-Nr.: 123555. doi:10.1016/j.energy.2022.123555

Frey, W.; Nick, P. (2022). Einsatz von Elektroimpulsen für die Biotechnologie von Mikroalgen. BioSpektrum, 28 (1), 94–96. doi:10.1007/s12268-022-1688-7

An, W.; Wang, Z.; Weisenburger, A.; Müller, G. (2022). Laser-induced fluorescence-dip spectroscopy of Rydberg states of xenon for electric field measurement in plasma. Review of scientific instruments, 93 (2), Article no: 023503. doi:10.1063/5.0064676

Gusbeth, C. A.; Frey, W. (2022). Integration of Pulsed Electric Fields in the Biorefinery Concept to Extract Microalgae Components of Interest for Food Industry. Pulsed Electric Fields Technology for the Food Industry. Ed.: J. Raso, 369–384, Springer Nature Switzerland AG. doi:10.1007/978-3-030-70586-2_12

Halim, R.; Papachristou, I.; Chen, G. Q.; Deng, H.; Frey, W.; Posten, C.; Silve, A. (2022). The effect of cell disruption on the extraction of oil and protein from concentrated microalgae slurries. Bioresource technology, 346, 126597. doi:10.1016/j.biortech.2021.126597

Krust, D.; Gusbeth, C.; Müller, A. S. K.; Scherer, D.; Müller, G.; Frey, W.; Nick, P. (2022). Biological signalling supports biotechnology – Pulsed electric fields extract a cell-death inducing factor from Chlorella vulgaris. Bioelectrochemistry, 143, 107991. doi:10.1016/j.bioelechem.2021.107991

3 Safety Research for Nuclear Reactors (NUSAFE): Transmutation -Liquid Metal Technology

Contact: Prof. Dr.-Ing. Georg Müller

Long-living high-level radioactive waste from existing nuclear power reactors should be transmuted in short-living radio nuclides using fast neutrons provided by a spallation target in an accelerator driven subcritical system or by a fast nuclear reactor. The objective is to reduce the final disposal time of high-level radioactive waste (plutonium, minor actinides) from some 10^6 years down to about 1000 years. Lead (Pb) and lead-bismuth (PbBi) are foreseen as spallation-target and coolant of such devices.

The aim of the institute's contribution is to develop advanced corrosion mitigation processes based on in-situ formation of protective alumina scales especially for parts under high loads like fuel claddings or pump materials in contact with liquid Pb or PbBi. Pulsed large area electron beams (GESA) are used to create aluminum containing surface alloys on steels. In addition, bulk alumina formers like FeCrAl, AFA (alumina forming austenitic steels) and HEA (high entropy alloys) are developed.

All tasks are embedded in European and international projects and cooperations like e.g., ILTROVATORE, ORIENT-NM, INNUMAT and EERA-JPNM.

The most relevant results obtained in the reporting period are presented briefly.

3.1 Material development and advanced corrosion mitigation strategies for heavy liquid metal-cooled nuclear systems

Contact: Dr. Alfons Weisenburger

3.1.1 Investigation of GESA facility

In order to investigate the plasma generated in the GESA facility during operation, laser induced fluorescence dip (LIF-dip) spectroscopy has been modified so that the distributions of the electric field can be determined in one measurement process. From this diagnostic, the length of the plasma sheath and the potential difference between the plasma and a conducting wall can be derived, allowing the plasma density to be determined. The result of measuring the distribution of the electric field with the LIF-Dip method is a two-dimensional pattern of a dip line, i. e. a decrease in LIF intensity, along which the amplitude of the electric field, which is linked to the resonance wavelength of a Rydberg level via the Stark effect, and the spatial coordinates are correlated. Most problems related to the interaction of a plasma with a conducting surface can be solved within the framework of a one-dimensional approximation. In this case, the interpretation of the measurement results by the LIF-dip method is simple: the Stark-shift (field amplitude) is a single-valued function of the spatial coordinate. In cases where this approximation is not possible, i.e. when the sheath length is comparable to the conducting wall, e.g. in the case of a thin point electrode used to generate a plasma by explosive emission, the coordinate associated with the electric field amplitude also

determines a spatial interpretation. Experimentally, two lasers are needed to create such a pattern: a pump laser induces the fluorescence of xenon atoms injected into the measurement area, while a probe laser provides a range of spatially distributed wavelengths that allow certain transitions of these atoms to higher energy levels (Rydberg levels). In the general case, the measured dip shape is determined by the intersection of the spatial distribution of Stark shifts associated with the electric field amplitude distribution and the spatial distribution of wavelengths of the probe laser. Fig. 3.1.1 shows the interpretation for a simulated point electrode used to generate a two-dimensional field with axial symmetry. The calibration plane of the probe laser (green) intersects the Stark shifts distribution along a certain three-dimensional (3D) curve (red points). The projection of the general 3D situation onto the spatial xy-plane, see Fig. 3.1.2, shows the theoretical dip whose shape is then superimposed on the measurement shown in Fig. 3.1.3, where it can be seen that the measured dip shape, dark region outside the point electrode boundary, contains the shape of the simulated one, indicating a match. The use of an inverse spectral distribution in the profile of the probe laser and a change the position of the resonant frequency of the "zero" field allow the measurement method to be to fine-tuned to the specific geometry of the conductor immersed in the plasma. The field along a specific line of interest, e. g. the axis of the electrode, can be reconstructed from the intersection points, assuming a spherical symmetry of the field distribution around the tip (see Fig. 3.1.4).

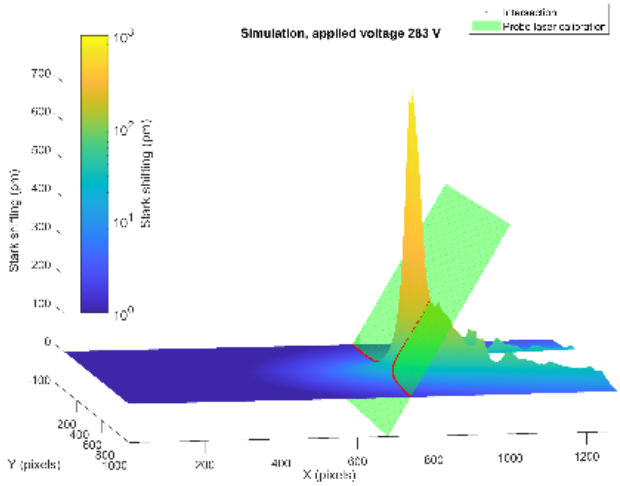

Fig. 3.1.1: Simulated Stark shifts' (electric field) spatial distribution around charged tip, intersected through the calibration function of probe laser

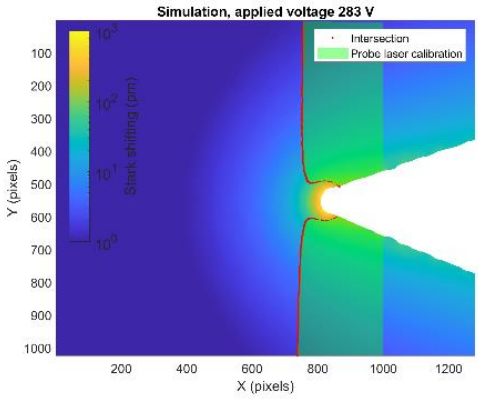

Fig. 3.1.2: Intersection line – "simulated DIP"

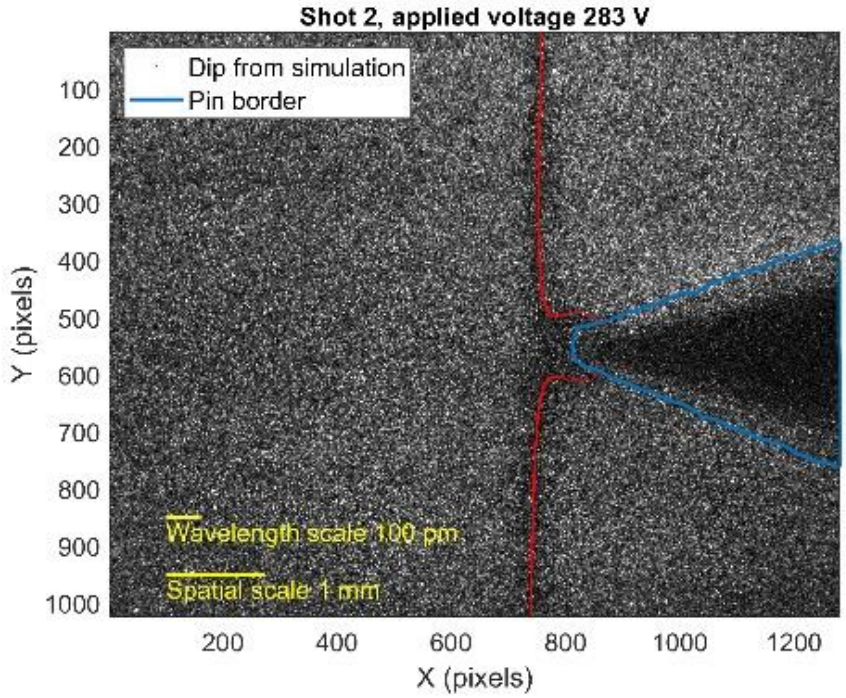

Fig. 3.1.3: Measured Stark shifts (dip region) compared with "simulated DIP" (red points).

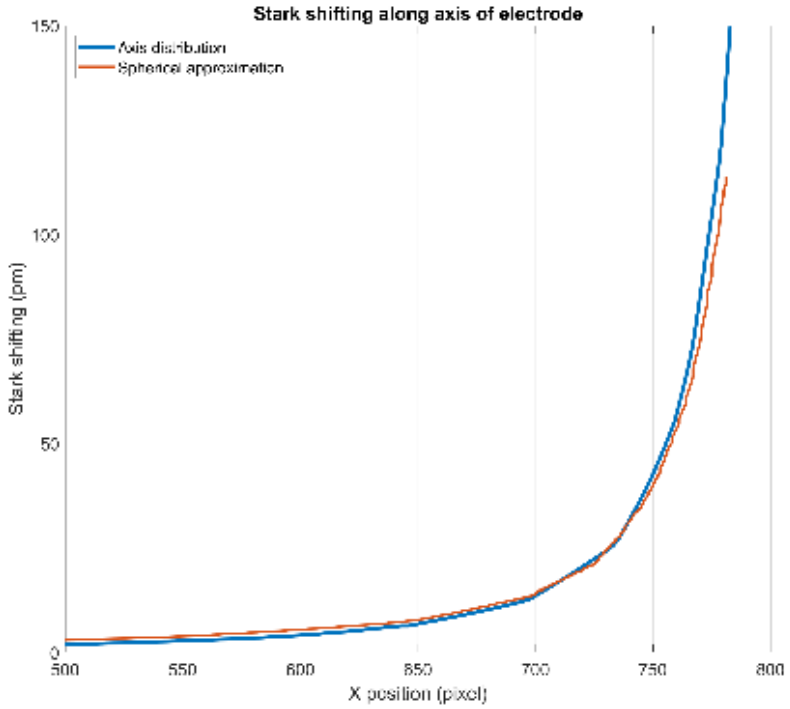

Fig. 3.1.4: Reconstruction of the field along the axis assuming the presence of spherical symmetry of the distribution near the tip

3.1.2 Erosion corrosion experiments in the CORELLA facility

The CORELLA facility designed for erosion corrosion experiments in liquid lead alloys with controlled oxygen content had been used in the previous years for various exposure experiments in flowing conditions. Although the maximum achieved velocity of the liquid metal was only around 1.6 m/s due to the specific design of the facility, the flow was characterized by a high level of turbulence. In order to reach a new flow regime with a much higher relative velocity between liquid metal and exposed samples, a new design for CORELLA-2 was searched in the reporting period. In contrast to the previous CORELLA, where the liquid metal was set in motion by a rotating inner cylinder and the samples were fixed at a stationary position, CORELLA-2 is planned to rotate the samples while keeping the flow of the liquid metal at a low level. Computational fluid dynamics simulations were performed to evaluate the expected performance of various designs. The numerical results predict relative velocities of 6 m/s and more.

3.1.3 Material development to mitigate corrosion

Exposure test in the frame of the EU project GEMMA showed that alumina forming coatings produced by pack cementation have a very good behaviour in liquid Pb with 10^{-7} wt% oxygen at 480 °C for up to 10000 h. Up to now we tested pack cementation samples from EU partners. A pack cementation facility was built up and first tests were conducted to further develop and optimize this process for application in Pb. Some of the first produced samples will be tested in the fretting facility available in-house.

Alumina coatings by pulsed laser deposition (PLD) are a kind of reference coating for lead-cooled nuclear facilities in Europe. Such coated samples always showed a slight reaction with Pb at the surface when exposed to oxygen containing Pb at elevated temperatures. Grazing incidence X-ray diffraction measurements now clearly showed that $Pb(Al_2O_4)$ is formed at the surface. In comparison to other crystalline Al_2O_3 layers that are known to be compatible in liquid Pb, these PLD coatings have an amorphous matrix. Whether this formed $Pb(Al_2O_4)$ layer has a long-term negative effect especially at higher temperatures needs to be further investigated.

Within the INNUMAT project, the composition of three different high alloyed AFA steels were defined on the basis of own experience and literature data. Extensive CALPHAD simulations with the thermodynamic software package Thermocalc finally form the basis for the selection of the three compositions to be produced by a partner institution within the INNUMAT project. Minimizing secondary phase formation (especially brittle phases) and stabilizing the austenitic matrix are in the focus of this approach. Main differences between the three alloys are the addition of W, Mn and the Al content.

Various Al-containing Max-phase coatings tested in molten Pb at 600 °C showed that scale formation strongly depends on the elements present in the Max-Phase. Cr_2AlC behaved best due to the formation of an Al_2O_3 scale with low amounts of Cr_2O_3. V_2AlC on the other hand, was almost completely consumed by the formed oxides. Both Ti containing Max-Phases showed the formation of mixed Al_2O_3 and TiO_2 scales that became less protective with higher Ti content.

Collaboration: SCK-CEN, ENEA, KTH, SANDIVK, CIEMAT, CEA, …

Funding: NUSAFE and EU-Projects

Journal Publications

Shi, H.; Azmi, R.; Han, L.; Tang, C.; Weisenburger, A.; Heinzel, A.; Maibach, J.; Stüber, M.; Wang, K.; Müller, G. (2022). Corrosion behavior of Al-containing MAX-phase coatings exposed to oxygen containing molten Pb at 600 °C. Corrosion Science, 201, Art.-Nr.: 110275. doi:10.1016/j.corsci.2022.110275

Malerba, L.; Al Mazouzi, A.; Bertolus, M.; Cologna, M.; Efsing, P.; Jianu, A.; Kinnunen, P.; Nilsson, K.-F.; Rabung, M.; Tarantino, M. (2022). Materials for Sustainable Nuclear Energy: A European Strategic Research and Innovation Agenda for All Reactor Generations. Energies, 15 (5), 1845. doi:10.3390/en15051845

4 Materials and Technologies for the Energy Transition (MTET): Power-based Fuels and Chemicals - Microwave Process Technology

Contact: Dr. Guido Link

Besides the activities on development of technologies and systems for the plasma heating in the FUSION Program, IHM is also in charge of research and development in the Power-based Fuels and Chemicals part of the MTET Program.

The main focus of IHM in this field of research is in plasma chemistry such as CO_2 dissociation or H_2 production by use of atmospheric plasmas sustained by high power microwaves, generated by innovative solid-state amplifiers. For this purpose, the power of plasma sources has been increased and further efforts were undertaken regarding plasma diagnostic and multiphysics modelling.

The expertise on microwave engineering and the existing industrial scale high power microwave infrastructure faces growing interest from industry and research. As a consequence, the research group is involved in several national and international joint research projects with objectives in various fields of applications. Further activities investigated the microwave assisted intermittent pultrusion of CFRP profiles (IMPULS), microwave assisted additive manufacturing with continuous carbon fiber reinforce thermoplastic filaments. In 2022 the IraSME project Phased-Array-Antenna for Microwave based Weed Control (PAMiCo) was started and a first waveguide-based antenna array was designed.

The successful presentation of our microwave assisted additive manufacturing technology on industrial trade fairs resulted in several contacts and initiatives for joint research proposals and technology transfer.

Within the highly multidisciplinary Helmholtz IVF project CORAERO (Airborn Transmission of SARS Coronavirus), which brings together scientists from virus biology, medicine, applied physics, chemistry, and engineering, IHM is involved in design and investigation of microwave-based concepts for inactivation of coronavirus.

Involved Staff: Jesus Nain Camacho Hernandez, Moritz Engler, Julia Hofele, Nanya Li, Guido Link, Dominik Neumaier, Volker Nuß, Adel Omrani Hamzekalaei, Thomas Seitz, Lucas Silberer, Sergey Soldatov.

4.1 Plasma Chemistry

Contact: Dr. Sergey Soldatov

To meet the demand on the Power-to-X technologies KIT-IHM, in tight collaboration with KIT-IMVT, contributes to the Helmholtz energy research program MTET (Materials and Technologies for the Energy Transition). We explore the reduction of CO_2 in atmospheric microwave plasma discharges for its subsequent conversion into valuable chemical precursors and synthetic fuels. If powered by renewable electricity, the process can be made carbon neutral. By sustaining a plasma in a compact coaxial reactor with short microwave pulses (several hundredth nanoseconds to several microseconds) rather than with

continuous microwave operation (CW) the conversion and efficiency of the process are found to be promoted. With using novel solid-state microwave generators from Trumpf Hüttinger Microwaves, which allow ultra-short pulsation down to the ns range and fine frequency control from 2.4 to 2.5 GHz, the effective gas temperature control by tuning of pulsation parameters was demonstrated in coaxial plasma torches.

The main efforts in 2022 were related to validate those results in a more powerful plasma torch such as the surfaguide (Fig. 4.1.1 a and b) microwave reactor. Compared to the before used coaxial plasma torch, surfaguides can be operated with larger microwave power levels in a range of several kW and results in significant higher conversion rates. Both, the conversion and efficiency of the process were studied in the pulsed and continuous wave (CW) plasma. First promising results show the importance of energy pulsations also in surfaguide (Fig. 4.1.1 c). In next steps, the afterglow system design is planned to be modified to enable a fast temperature quenching. This can suppress backreaction and achieve a better conversion rates into CO.

For tailoring advanced plasma scenarios and for understanding of physics behind, the use of plasma diagnostics is of highest importance. For this purpose, we have successfully implemented a time resolved optical emission spectrometer (OES) which next will be complemented by a time resolved Fourier-transform infrared (FTIR) spectrometer. For investigation of plasma electron density, the microwave interferometry operating in a frequency range from 47 GHz up to 77 GHz was developed. Ultra-fast imaging synchronized with plasma pulsations enabled to follow the time evolution of the light pattern emitted by the CO_2 plasma.

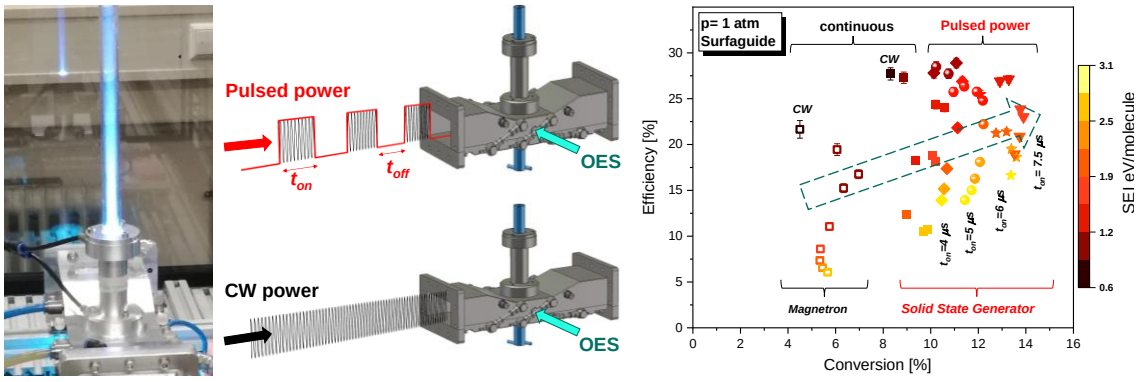

a) b) c)

Fig. 4.1.1: Burning CO_2 plasma in surfaguide (a), principle of sustaining plasma with pulsed and continuous microwave power (b), efficiency vs. conversion for CO_2 splitting in pulsed and continuous wave operation (c).

4.2 IMPULS

Contact: M.Sc. Moritz Engler

Pultrusion is a manufacturing process for the continuous production of fiber-reinforced polymer profiles, where reinforcing fibers are impregnated with a thermoset resin and then pulled though a heated die, which forces the material into the desired cross section and simultaneously cures the resin. The nature of the process limits it to constant cross section profiles which are straight or of constant radius.

The IMPULS Project aims to mitigate this limitation by developing a microwave powered pultrusion process. As the microwave heating allows to selectively heat the profile in the otherwise cold tool, the degree of cure of the profile can be changed instantaneously by changing the microwave power. By alternating between fully cured and uncured segments, the profile can be locally deformed, opening the process to a variety of new applications. Within the scope of the Project two microwave applicator concepts were build and tested. The first design is based on a preexisting waveguide applicator which was modified to concentrate microwave heating to a small area within the tool (see Figure 4.2.1 top). The second applicator has a coaxial design which allows reduction of the contact area between the tool and the heated pultrusion profile (see Figure 4.2.1 bottom). Both applicators were used for experiments and could successfully generate the desired transitions between cured and uncured segments, with small transition lengths. The second design achieved better energy efficiency, as there is significantly less thermal loss due to the reduced contact area between the hot pultrusion profile and the cold tool. In addition, this tool showed a reduced risk for the pultrusion profile to stick to the tool and damage the ceramic forming die.

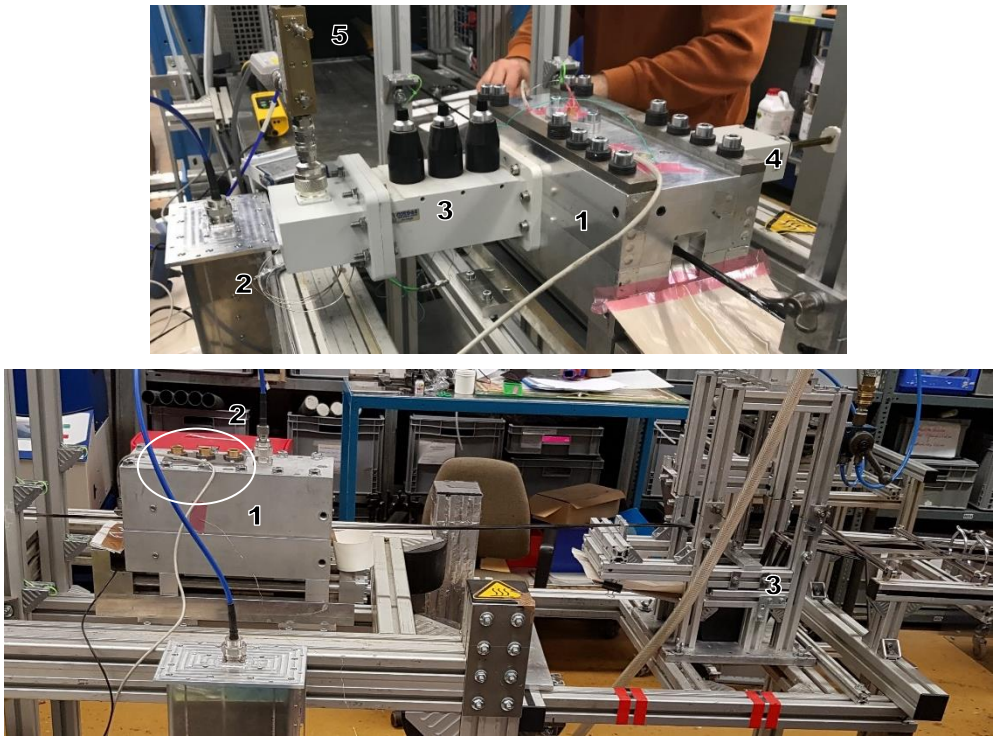

Figure 4.2.1: (top) Pultrusion line with waveguide-based applicator (1), solid state microwave source (2), waveguide tuners (3,4) and caterpillar pulling unit (5). (bottom) Coaxial pultrusion tool (1) with integrated tuners (2) and resin impregnation bath (3).

Funding: ZIM cooperation project, support code: ZF4204604BL8

4.3 3D Microwave Printing of Composites

Contact: Dr. Guido Link

Many industrial sectors, such as the automotive and aviation industries, rely on fiber reinforced composites as a high-tech material. Using additive manufacturing (known as 3D printing) techniques and their freedom of design, a plastic matrix with continuous fiber reinforcement are used to create lightweight components with high strength. However, the known 3D printing processes in terms of continuous reinforcements are very limited regarding filament diameter, printing speed and structure complexity due to the bottlenecks of the heating source and printing control technologies. An innovative concept, using microwave heating of pre-impregnated and continuous carbon fiber reinforced filaments, allows uniform and rapid heating of even large diameter filaments. Thus, any limit of printing speed given in conventional printing nozzle due to limited thermal conductivity of polymer-based filaments can be overcome. So far filaments with matrix materials such as Polylactic Acid (PLA), Polyamide (PA) and Polyetheretherketone (PEEK) have been successfully tested.

In the meantime, a patent has been granted for this technology. A prototype of the printer was exhibited at JEC World in Paris the leading international composite show as well as at the Hanover Fair, one of the world largest trade fairs and generated a considerable amount of academic as well as industrial interest.

This has already led to various concrete cooperation talks and the first concrete joint project applications have been submitted.

Fig. 4.3.1: 3D microwave printing technology of KIT was presented at JEC World in Paris the leading international composite show

Funding: Alexander von Humboldt Research Project, YIG Prep Pro

4.4 CORAERO

Contact: MSc. Jesus Nain Camacho Hernandez

The COVID-19 pandemic was a global pandemic caused by the respiratory syndrome coronavirus (SARS-CoV-2). According to the World Health Organization (WHO) by may 2023 there have been around 687 million confirmed cases of COVID-19, including 6 million deaths. There is a clear need to develop novel and efficient technologies to prevent virus tranmission and thus keep future pandemics under control. The Helmholtz CORAERO project brings together a multidisciplinary group of scientists from virus biology, medicine, applied physics, chemistry, and engineering to understand virus spreading through aerosols and designing technical and administrative measures for mitigation and virus control. The IHM participates in the CORAERO project, by researching on air purification systems that use microwave radiation to reduce virus load in closed spaces, such as public and private rooms. Extracorporeal inactivation of the virus addresses treatment of airborne virus from droplets and aerosols. Among the physical inactivation strategies, structural damage of the virus by heat and electric fields of moderate strenght are currently the approaches of choice as they can be achieved within the microwave frequency spectrum.

For air purification systems two microwave applicator concepts are being considered. An initial prototype of the applicator, comprising a resonant cavity, has been developed and is depicted in Figure 4.4.1.a. The design of the cavity was developed using numerical calculations. The specific goal was to achieve a uniform electric field of moderate strength (E-field > 10^5 Vm^{-1}) along the air duct. This pathway serves as a conduit for virus-laden aerosols, enabling us to conduct experimental investigations aimed at inducing persistent structural damage in viruses. In addition, an experimental setup has been mounted in a BioSafety Level 3 laboratory at our cooperation partner Forschung Helmholtz Zentrum München, Institut für Virologie, which enable carrying testing of SARS-CoV-2. The experimental design also allows to control various parameters that could potentially impact virus inactivation. Concurrently, efforts are being undertaken to adapt the resonance cavity to this experimental setup and to integrate a powerfull solid-state microwave source. On the other hand, a second microwave applicator is under consideration for evaluating heat inactivation of viruses. This concept relies on the use of selective and energy-efficient microwave heating of aerosols captured in filter media. The heating approach targets the sterilization of pathogenic aerosols, a crucial step in preventing virus re-entrainment into the exhaust air. The considered filter media specifically focuses on woven and non-woven filters (see Figure 4.4.1.b) that comprise HEPA-grade filters. HEPA filters are commonly used in ventilation systems to mitigate the risk of virus propagation. In specific, the effective permittivity of fibers has been investigated. Various models have been developed considering the orientation and geometry of the microstructure of fibers, recognizing their inherent anisotropy.

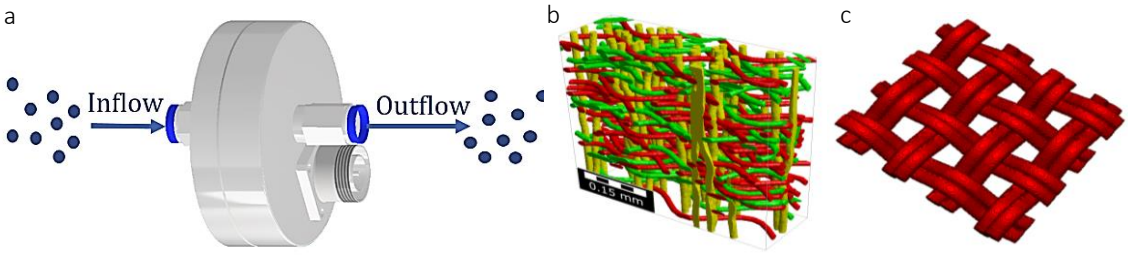

Fig. 4.4.1: (a) Microwave applicator intended for virus inactivation using E-fields, and (b) non-woven and (c) woven fabrics, which have been studied for determining effective permittivity and for the application of microwave heating.

Funding: HGF Initiative and Networking Fund, www.coraero.de

4.5 PAMiCo

Contact: M.Sc. Adel Omrani Hamzekalaei

In farming production, weeds compete with crops for sunlight, space, nutrients, water, and CO_2 and can significantly impact crop products worldwide. Dense weed growth can make harvesting very difficult and reduce it significantly. Even though an estimated 3 billion kg of pesticides is currently applied worldwide, it is estimated that 37 % of global crop production is still lost. 13 % of this is due to insects, 12 % to plant pathogens, and 12 % to weeds.

Controlling and demolition of the distribution of weeds in a crop field is vital to increase the production rate. Weed control by microwaves is supposed to be an environmentally friendly method for replacing chemical and pesticide methods, which are no longer acceptable from an ecological point-of-view.

As part of an IraSME funded project, IHM is in charge of development and demonstration of a novel microwave antenna. The main objective within the project regarding the microwave technologies is the optimization of treatment speed, reduction of treatment frequency, lower energy demand and the possibility to decarbonize the required energy. Conducting the microwaves to the location of unwanted plant, can lead to the bursting of cells inside the unwanted plant at high power densities, as opposed to steaming, which is a surface heat treatment only with low energy efficiency. It should be mentioned, the location of this unwanted plants is determined using an optical sensor. In Fig. 4.5.1, a slotted waveguide phased array antenna, designed for 5.8 GHz is shown. Different associated phase distributions are applied to each element of the array to evaluate the beam steering by simulation approach. As can be seen in Fig. 4.5.2, by exciting the elements of the phased array antenna using different phase shifts, the desired steerability can be achieved to focus the electromagnetic beam on the location of the weed.

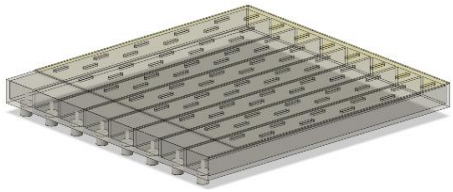

Fig. 4.5.1: Schematic of the SWA antenna

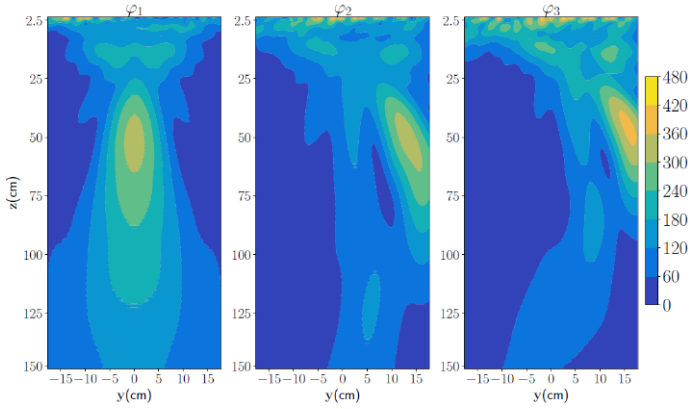

Fig. 4.5.2: Steering of the proposed NFF phased-array antenna for the different phase distribution.

Funding: ZIM cooperation project; support code KK5431301DF1

Journal Publications

Li, N.; Link, G.; Jelonnek, J. (2022). Electroplating of 3D Printed Plastic Component for the Application of Microwave Filter. 2022 IEEE MTT-S International Microwave Workshop Series on Advanced Materials and Processes for RF and THz Applications (IMWS-AMP), Guangzhou, CHN , November 13 - 15, 2022, 1–3, Institute of Electrical and Electronics Engineers (IEEE). doi:10.1109/IMWS-AMP54652.2022.10106897

Omrani, A.; Yadav, R.; Link, G.; Lähivaara, T.; Vauhkonen, M.; Jelonnek, J. (2022). Multistatic Uniform Diffraction Tomography Derived Structural-Prior in Bayesian Inversion Framework for Microwave Tomography. IEEE Transactions on Computational Imaging, 8, 986–995. doi:10.1109/TCI.2022.3212835

Camacho Hernandez, J. N.; Link, G.; Schubert, M.; Hampel, U. (2022). Experimental Study of a Compact Microwave Applicator for Evaporation of Airflow-Entrained Droplets. Materials, 15 (19), Article no: 6765. doi:10.3390/ma15196765

Hofele, J.; Engler, M.; Link, G.; Jelonnek, J. (2022). Combination of Scattering Matrix Code and Process Model to Optimize a Microwave Applicator Suitable for the Stabilization of PAN Fibers. 2022 14th German Microwave Conference (GeMiC), Ulm, 16-18 May 2022, 232–235, Institute of Electrical and Electronics Engineers (IEEE).

Omrani, A.; Yadav, R.; Link, G.; Jelonnek, J. (2022). A Multistatic Uniform Diffraction Tomography Algorithm for Microwave Imaging in Multilayered Media for Microwave Drying. IEEE Transactions on Antennas and Propagation, 70 (10), 9583–9595. doi:10.1109/TAP.2022.3177495

Hosseini, M.; Kaasinen, A.; Link, G.; Aliyari Shoorehdeli, M.; Lähivaara, T.; Vauhkonen, M. (2022). Tomography-assisted control for the microwave drying process of polymer foams. Journal of Process Control, 114, 16–28. doi:10.1016/j.jprocont.2022.03.011

Camacho, J. N. Hernandez; Link, G.; Schubert, M.; Hampel, U. (2022). Novel Mixing Relations for Determining the Effective Thermal Conductivity of Open-Cell Foams. Materials, 15 (6), Art.-Nr.: 2168. doi:10.3390/ma15062168

Yadav, R.; Omrani, A.; Link, G.; Vauhkonen, M.; Lahivaara, T. (2022). Correlated Sample-based Prior in Bayesian Inversion Framework for Microwave Tomography. IEEE Transactions on Antennas and Propagation, 70 (7), 5860–5872. doi:10.1109/TAP.2022.3145433

Hofele, J.; Link, G.; Jelonnek, J. (2022). Reaction Kinetics and Process Model of the Polyacrylonitrile Fibers Stabilization Process Based on Dielectric Measurements. Materials, 15 (3), 1222. doi:10.3390/ma15031222

Soldatov, S.; Carbone, E.; Kuhn, A.; Link, G.; Jelonnek, J.; Dittmeyer, R.; Navarrete, A. (2022). Efficiency of a compact CO2 coaxial plasma torch driven by ultrafast microwave power pulsing : Stability and plasma gas flow dynamics. Journal of CO2 Utilization, 58, Art.-Nr.: 101916. doi:10.1016/j.jcou.2022.101916

Appendix

Equipment, Teaching Activities and Staff

IHM is equipped with a workstation cluster and a large number of experimental installations: KEA, KEA-ZAR, three GESA machines, eight COSTA devices, one abrasion and one erosion teststand, a gyrotron test facility including a microwave-tight measurement chamber and two teststands for gyrotrons, one compact technology gyrotron (30 GHz, 15 kW CW), several 2.45 GHz applicators of the HEPHAISTOS series, one 0,915 GHz, 60 kW magnetron system, one 5.8 GHz, 3 kW klystron installation and a low power microwave laboratory with several vectorial network analysers, a plasma laboratory with 2,45 GHz atmospheric plasma sources up to 6 kW and a laboratory for microwave assisted 3D printing of continuous fibre reinforced filaments.

The project FULGOR, targeting for a renewal of the KIT gyrotron teststand is progressing. In 2013, an agreement on the project structure including the involvement of the KIT project and quality management has been achieved. The final start of the procurement of the equipment was in 2014 whereas the first initial test of operation was starting in 2021.

Prof. John Jelonnek, strongly supported by Dr.-Ing. Alexander Marek has continued to teach the lecture course entitled “High Power Microwave Technologies (Hochleistungsmikrowellentechnik)” for Master students. In 2022, additionally, Prof. John Jelonnek has started to teach part of the lecture course “Lineare elektrische Netze (LEN)” for undergraduate students. The lecture course LEN is coordinated by Prof. Sebastian Kempf of the Institute of Micro- and Nanoelectronics Systems (IMS). Prof. Georg Müller has continued to teach the lecture on “Pulsed Power Technologies and Applications” at KIT. Dr. Gerd Gantenbein has been teaching the part “heating and current drive” of the lecture “Fusionstechnologie B” by Prof. R. Stieglitz, IFRT. Dr.-Ing. Martin Sack hold the lecture course “Elektronische Systeme und EMV”.

At the turn of the year 2022/2023 the total staff with regular positions amounted to 38 (20 academic staff members, 10 engineers and 8 technical staff member and others). Additionally, 9 academic staff members, 2 engineer and 1 technical staff members (and others) were financed by acquired third party budget.

In course of 2022, 2 guest scientists, 14 doctoral students (1 of KIT-Campus South, 10 of KIT-Campus North, 3 others), 2 DHBW students, 4 trainees in the mechanical and electronics workshops worked at IHM. 2 Master students, 2 Bachelor students, 15 student assistants and 3 Research internships were supervised at IHM during 2022.

Strategical Events, Scientific Honors and Awards

Longlasting Co-operations with Industries, Universities and Research Institutes

- Basics of the interaction between electrical fields and cells (Bioelectrics) in the frame of the International Bioelectrics Consortium with Old Dominion University Norfolk, USA; Kumamoto University, Japan; University of Missouri Columbia, USA; Institute Gustave-Roussy and University of Paris XI, Villejuif, France; University of Toulouse, Toulouse, France, Leibniz Institute for Plasma Science and Technology, Greifswald, Germany.

- Cooperation on the technological development of a sodium liquid metal battery as an electrical storage device with DLR and the Huazhong University of Science and Technology – HUST in Wuhan (China).

- Development of protection against corrosion in liquid metal cooled reactor systems in the following EU-Projectes: GETMAT, IL TROVATORE (Partner: CEA, ENEA, SCK-CEN, CIEMAT).

- Development of large area pulsed electron beam devices in collaboration with the Efremov Institute, St. Petersburg, Russia (on hold).

- Development of advanced 1.5 MW gyrotrons, gyrotron for multi-purpose operation and new gyrotron control techniques for the ECRH System at the stellarator Wendelstein W7-X in collaboration with the Max-Planck-Institute for Plasmaphysics (IPP) Greifswald.

- Development of the European gyrotrons for ITER in the frame of the European GYrotron Consortium (EGYC) and coordinated by Fusion for Energy (F4E). The other members of the Consortium are EPFL Lausanne, Switzerland, CNR Milano, Italy, ENEA, Frascati, Italy, HELLAS-Assoc. EURATOM (NTUA/NKUA Athens), Greece. The industrial partner is the microwave tube company Thales Electron Devices (TED) in Paris, France.

- Development of 105 GHz 1 MW gyrotrons for WEST in collaboration with EPFL, Lausanne, Switzerland and CEA, Cadarache, France.

- In frame of EUROfusion, collaboration with EPFL Lausanne, Switzerland, CNR Milano, Italy, ENEA, Frascati, Italy, HELLAS-Assoc. EURATOM (NTUA/NKUA Athens), Greece and the industrial partner Thales Electron Devices (TED), Paris, France to develop gyrotrons for future European DEMOstration fusion power plant. EUROfusion is a consortium of national fusion research institutes located in the European Union, the UK, Switzerland and Ukraine.

- Development of Microwave Systems of the HEPHAISTOS Series for materials processing with microwaves with the Company Vötsch Industrietechnik GmbH, Reiskirchen.